Intermediate–mass–ratio–inspirals in the Einstein Telescope. II. Parameter estimation errors.

E. A. Huerta and Jonathan R. Gair
*Institute of Astronomy, Madingley Road, CB3 0HA Cambridge, UK**
(Dated: November 2, 2010)

We explore the precision with which the Einstein Telescope (ET) will be able to measure the parameters of intermediate–mass–ratio inspirals (IMRIs), i.e., the inspirals of stellar mass compact objects into intermediate-mass black holes (IMBHs). We calculate the parameter estimation errors using the Fisher Matrix formalism and present results of a Monte Carlo simulation of these errors over choices for the extrinsic parameters of the source. These results are obtained using two different models for the gravitational waveform which were introduced in paper I of this series. These two waveform models include the inspiral, merger and ringdown phases in a consistent way. One of the models, based on the transition scheme of Ori & Thorne [1], is valid for IMBHs of arbitrary spin, whereas the second model, based on the Effective One Body (EOB) approach, has been developed to cross–check our results in the non-spinning limit. In paper I of this series, we demonstrated the excellent agreement in both phase and amplitude between these two models for non–spinning black holes, and that their predictions for signal–to–noise ratios (SNRs) are consistent to within ten percent. We now use these waveform models to estimate parameter estimation errors for binary systems with masses $1.4M_\odot$+$100M_\odot$, $10M_\odot$+$100M_\odot$, $1.4M_\odot$+$500M_\odot$ and $10M_\odot$+$500M_\odot$ and various choices for the spin of the central intermediate–mass black hole (IMBH). Assuming a detector network of three ETs, the analysis shows that for a $10M_\odot$ compact object (CO) inspiralling into a $100M_\odot$ IMBH with spin $q = 0.3$, detected with an SNR of 30, we should be able to determine the CO and IMBH masses, and the IMBH spin magnitude to fractional accuracies of $\sim 10^{-3}$, $\sim 10^{-3.5}$ and $\sim 10^{-3}$, respectively. We also expect to determine the location of the source in the sky and the luminosity distance to within ~ 0.003 steradians and $\sim 10\%$, respectively. We also compute results for several different possible configurations of the third generation detector network to assess how the extrinsic parameter determination depends on the network configuration.

PACS numbers:

I. INTRODUCTION

Significant progress has been made over the last few years in the quest for the first direct detection of gravitational waves (GWs). During the most recent published data–taking run of the ground-based GW detectors five instruments were operational. The three LIGO detectors started their Science Run 5 (S5) in November 2005 [2]. Subsequently, the GEO 600 detector [3] joined the S5 run in January 2006 and the Virgo detector [4] started its Science Run 1 (VSR1) in May 2007. All five detectors worked in triple–coincidence until the beginning of October 2007. The data set gathered during the first calendar year of the LIGO S5 (S5y1) run has already been analysed for GW burst signals in the frequency band 64–6000 Hz [5],[6] although this failed to identify any GW candidates. The data collected during the rest of the S5/VSR1 run, referred to as "S5y2/VSR1", is the first long–term observation with the worldwide network of interferometric detectors. An all–sky search for GW burst signals has also been conducted on S5y2/VSR1. The performance of this search has improved by more than one order of magnitude both in the analyzed frequency bandwidth and the level of instrumental noise [7]. Even though the S5y2/VSR1 search also failed to identify plausible GW candidates, this analysis benefited from substantially improved data quality and analysis algorithms relative to earlier searches, e.g., LIGO S4 in 2004 [8] and the first year of LIGO S5 in 2005–2006 [5],[6]. For instance, S5y2/VSR1 combined with the S5y1 results, which had comparable observation time, has yielded an improved upper limit on the rate of gravitational wave bursts of 3.75 events per year for the 64–2048 Hz band, and 5.4 per year for higher–frequency bursts up to 6 kHz. These improved upper limits are more than an order of magnitude better than the upper limits from S4 or S5 events per year [7]. Towards the end of this year, the LIGO and Virgo detectors will be taken offline and the upgrade to the Advanced detectors will begin. It is expected that Advanced LIGO and Virgo will increase the detection range of future searches by as much as a factor of 10, so that the monitored volume of the universe would increase by a factor of ~ 1000. If this is achieved, the detection of GW signals from binary mergers should become

*Electronic address: eah41@ast.cam.ac.uk; Electronic address: jgair@ast.cam.ac.uk

routine.

Seismic noise limits the sensitivity of LIGO, Virgo, GEO and their advanced configurations to frequencies $\gtrsim 10$ Hz. This in turn means that ground–based advanced detectors will not be sensitive to signals from coalescing binaries with mass in the $\sim 100M_\odot - 1000M_\odot$ range, since the associated gravitational radiation will be in the 0.1–10 Hz band. This frequency band is also above the sensitivity band of the space-based gravitational wave detector LISA, which is sensitive in the $0.1\text{mHz} - 0.1\text{Hz}$ range. A GW detector operating in this frequency band may shed some light on astrophysical processes that took place at early cosmic times. Over the last decade evidence has accumulated for the existence of black holes of intermediate mass (IMBHs). Ultraluminous X-ray sources have been observed that are not associated with AGN, but which have fluxes which would imply accretion rates many times the Eddington limit if the accreting object had a mass $M \lesssim 20M_\odot$. In addition, the stellar kinematics in the centres of several globular clusters, e.g., M15 in the Milky Way, and G1 in M31, show evidence for an excess of dark mass in their centres. A full review of the observational evidence for IMBHs can be found in [9]. Intermediate-mass black holes could form through two distinct channels. Firstly, they could form in the early universe through the collapse of massive, low–metallicity "Population III" stars. In the cold dark matter framework, galaxies formed through a series of mergers between initially low-mass objects that condensed at early cosmic times. The black holes seen today similarly grew through a combination of mergers and accretion, from initial seeds. In the Pop-III star model, the initial seed black holes are of intermediate mass, $100M_\odot - 1000M_\odot$, but the initial seeds could also have been 'heavy', $\sim 10^5 M_\odot$. The discovery of IMBHs present at early cosmic times would be a strong discriminator between these alternatives. The second channel for IMBH formation is the runaway collision of stars in the centre of a dense stellar cluster [10], [11]. If IMBHs are found to be common in globular clusters, this would be an important probe of the processes taking place in such dense stellar systems. Observations in the electromagnetic spectrum will improve in coming years, but it is likely that the first robust mass determination, and hence the first convincing proof of the existence of IMBHs, will come from GW observations [9]. A GW detection of an IMBH at high redshift will lend strong support to the light seed scenario for structure formation, no matter how that IMBH was formed, and the detection of large numbers of IMBHs in globular clusters would indicate that runaway stellar collisions occur generically in such environments.

In order to do this science, we require a detector in the $1 - 10\text{Hz}$ frequency range. A design study is ongoing within Europe at the moment for a third-generation ground-based GW detector, the Einstein Telescope (ET), to follow on from the Advanced detectors. The target is a sensitivity ten times better than that of the Advanced interferometers, and a frequency sensitivity band that stretches down into the 1-10 Hz range. The ET will be an outstanding tool to address problems in fundamental physics, cosmology and astrophysics. It will have the capability to do the same type of science as the Advanced detectors, but with better sensitivity, and to do new science through the detection of sources in the $1 - 10\text{Hz}$ band. The IMBH sources fall into this second category, and in this paper we will continue to explore the GWs generated from the mergers of IMBHs with lower mass compact objects, namely neutron stars or stellar–mass black holes, so-called intermediate–mass–ratio inspirals (IMRIs).

For ET to detect GWs generated during IMRIs, we need accurate waveform models in the intermediate-mass-ratio regime, which are not yet available. Source modelling is an ongoing effort that has been successful for comparable-mass-ratio and extreme-mass-ratio systems. In the comparable-mass regime post–Newtonian (PN) theory has provided waveform templates for the inspiral phase evolution, while numerical relativity (NR) can now be used to model the final few cycles of inspiral and the plunge and merger [12]. At the other extreme we have extreme–mass–ratio inspirals (EMRIs) with mass ratios $\sim 10^{-6}$–10^{-4}. In this regime, the smaller object may complete several hundred thousand orbits at a velocity that is a significant fraction of the speed of light before crossing the horizon of the central supermassive black hole. Modelling the gravitational radiation of EMRIs using NR is presently impractical due to the excessive computational cost of simulating so many orbits. However, we can model these systems accurately using Black Hole Perturbation Theory, treating the mass–ratio as a small expansion parameter [13], [14]. The sources we shall now examine lie somewhere between these two regimes. In paper I of this series [15] we developed two waveform models that include the inspiral, merger and ringdown phases using the best of what is currently available. We discussed in detail how to construct a complete waveform for CO inspirals into spinning IMBHs using the scheme developed by Ori & Thorne [1]. In order to build up confidence in our waveform model, we also used the effective–one–body (EOB) approach [16, 17] to construct a different waveform model for non–spinning systems. The two models showed an excellent level of agreement in both the phase and the amplitude. We used these models to compute signal–to–noise ratios (SNRs) for a selection of IMRI systems. We cross–checked our results for the non–spinning systems and found that the two models made predictions which were consistent to better than ten percent. We used these SNRs to estimate the number of events that could be detected by ET and found that this could be as many as hundreds of IMRI coalescences per year up to redshift $z \sim 5$ if the systems are light, and up to as many as tens of IMRI coalescences up to redshift $z \sim 0.3$ if the systems are massive [15]. In this paper, we shall address a complementary problem, namely to calculate the accuracies with which an ET network will be able to estimate parameters of any IMRI sources that are detected. This is an important problem because an accurate determination of the masses of a merging binary and a measurement of the luminosity distance at which the merger is taking place

will be useful for extracting science from the observations, e.g., choosing between light-seed and heavy-seed models of structure formation. Since the binary systems are typically short–lived, a single ET will not be able to localise a source on the sky, so we will assume the existence of a network of detectors. We will consider several different network configurations in order to assess how this affects the science, which will be useful input for future design decisions.

This paper is organized as follows. In Section II we outline the assumptions we shall adopt for the detector and detector networks, and describe the binary systems to be used in the subsequent analysis. In Section III we present a brief description of the waveform models that will be used to estimate parameter errors. In Section IV we summarise some basics of signal analysis that will be relevant for our studies and briefly describe the noise model we shall use for our studies, i.e., the official ET noise curve, "ET B" [18]. In Section V we will use our waveform models, as described in paper I [15], to estimate the parameter errors that would arise due to detector noise, using the Fisher Matrix formalism. We present results for a 3–ET network for 12 sample IMRI systems and use four of these to explore how the results change under alternative configurations of the network. Finally, we summarize our work and discuss the implications of these results in Section VI.

II. ASSUMPTIONS

A. Einstein Telescope Design

We make the same assumptions about the ET sensitivity that we made in paper I. The design sensitivity is usually quoted for a single right-angle interferometer with 10km arms. In this paper we shall use the most up-to-date sensitivity curve for ET that is currently available, referred to as "ET B" [18]. The corresponding amplitude spectrum is plotted in Figure 1.

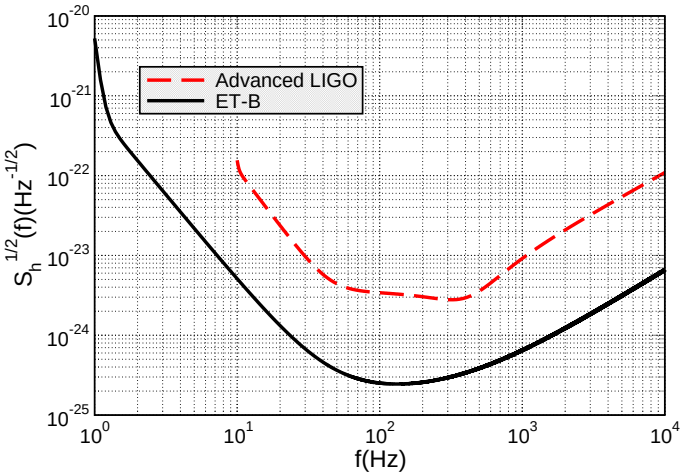

FIG. 1: Sensitivity curve for the Einstein Telescope, as described in the text. The Advanced LIGO noise curve is also shown for reference.

An analytic fit to the ET–B spectral density is given by [18]

$$S_h^{1/2}(f) = \begin{cases} S_0^{1/2}\left[a_1 x^{b_1} + a_2 x^{b_2} + a_3 x^{b_3} + a_4 x^{b_4}\right] & \text{if } f \geq f_s, \\ \infty & \text{if } f < f_s, \end{cases} \tag{1}$$

where $x = f/f_0$, f stands for the frequency, $f_0 = 100$Hz, $S_0 = 10^{-50}\text{Hz}^{-1}$, and f_s is a low frequency cut–off that can be varied, and below which the sensitivity curve can be considered infinite for practical purposes. The various coefficients take the values

$$\begin{aligned} a_1 &= 2.39 \times 10^{-27}, & b_1 &= -15.64, \\ a_2 &= 0.349, & b_2 &= -2.145, \\ a_3 &= 1.76, & b_3 &= -0.12, \\ a_4 &= 0.409, & b_4 &= 1.10. \end{aligned} \tag{2}$$

It is expected that ET will operate with an improved sensitivity over advanced detectors in the frequency range 1–10 Hz. Assuming a low frequency cut–off of 1Hz might be too optimistic as ET may only have sensitivity down to ~ 3Hz or higher. Given this uncertainty, we adopt a conservative approach and use a low frequency cut–off of 5Hz.

We take the response of a "single ET" to be that of two right-angle interferometers, coplanar and colocated but offset from one another by 45°. The currently favoured ET design is for a triangular configuration comprising three 10km detectors with 60° opening angles in a single facility, as this has lower infrastructure costs [19]. The response of the triangular configuration contains the same information as that of the two right-angle interferometers (assuming uncorrelated noise), but its sensitivity is a factor of $3/(2\sqrt{2}) \approx 1.06$ higher. As in paper I, we ignore this factor since it is small compared to other uncertainties in the design.

IMRI signals are short–lived, so to enable extrinsic parameter estimation we need to assume the existence of a network of detectors. Our optimistic reference case will be a network of three detectors, each with the sensitivity of a single ET. We assume the detectors are sited at the geographic locations of Virgo, LIGO Livingston and in Perth (Australia). This configuration is highly optimistic, so we shall also explore how parameter estimation accuracies are modified for four additional network configurations, C1-C4. These configurations are, C1: one ET at the geographic location of Virgo; C2: as configuration C1 plus a right–angle detector at the location of LIGO Livingston; C3: as configuration C1 plus another ET at the location of LIGO Livingston; and C4: as configuration C2 plus another right–angle detector in Perth. We will denote the reference 3-ET network as configuration C5.

B. Sample IMRI systems

We will present parameter estimation errors for the same twelve binary systems that we used in paper I [15]. These correspond to all possible combinations between four sets of component masses — $1.4M_\odot + 100M_\odot$, $1.4M_\odot + 500M_\odot$, $10M_\odot + 100M_\odot$, and $10M_\odot + 500M_\odot$ — and three different values for the spin of the central IMBH — $q = 0$, 0.3, 0.9. The mass and spin distributions of IMBHs are extremely uncertain, so we choose these systems to cover the range of possibilities. The small object masses are chosen to represent mergers with black holes ($10M_\odot$) or neutron stars ($1.4M_\odot$).

As discussed in paper I [15], if IMBHs gain mass through a series of minor mergers with smaller objects, then their angular momenta will undergo a damped random walk. Under such evolution, it is expected that IMBHs in the mass range $100M_\odot - 1000M_\odot$ would end up with moderate spin parameters, $q \sim 0.3$ [20]. We will regard this as the 'typical' case and will use only that spin value when we explore how the parameter estimation accuracies depend on the network configuration. For the other spin parameters, we shall only quote results for the optimistic 3 ET network and these should be regarded as 'best-case' values for the accuracy with which we may be able to determine the parameters.

III. IMRI WAVEFORM MODELLING

We will use the two waveform models developed in paper I of this series to explore the precision with which ET will be able to determine the source parameters using the various network configurations. Full details of the waveforms are given in [15], but we briefly summarise the models here.

Both waveform models include inspiral, merger and ringdown in a consistent way. We model the inspiral phase evolution, in both models, using the "numerical kludge" waveform model described in [13]. The "numerical kludge" approach consists of computing the orbital trajectory that the inspiralling body follows in the Boyer–Lindquist coordinates of the Kerr spacetime of the central black hole. We assume an adiabatic evolution in which the inspiralling body is moving on a geodesic and use the fluxes of energy E and angular momentum L_z derived in [21] to evolve the parameters of the geodesic. In this paper, we restrict our attention to circular–equatorial geodesics. Subsequently, we numerically integrate the geodesic equations along this inspiral trajectory and obtain the Boyer–Lindquist coordinates of the small object as a function of time. Finally, we construct a gravitational waveform from the inspiral trajectory using a flat–spacetime wave–emission formula. This scheme, which was developed for the modelling of EMRI systems for LISA, has several useful features: a) the waveforms have been checked against more accurate, Teukolsky–based, waveforms for test-particles on geodesic orbits and the overlap exceeds 0.95 over a large portion of the parameter space [13]; b) they are computationally inexpensive; c) conservative self–force corrections to this model have been derived [14] for Kerr circular–equatorial orbits at 2PN order. Nonetheless, this model is, at present, incomplete in several ways, e.g., conservative corrections are not yet known for generic orbits; the phase space trajectories are approximate, although they have been matched to Teukolsky based evolutions; and the waveform is constructed from the trajectory using a flat–spacetime wave–emission formula. Nevertheless, this approach should capture the main features of the inspiral waveform accurately.

The two models differ in their treatment of the plunge and merger phases. The first model, valid for IMBHs of arbitrary spin, employs the transition scheme developed by Ori & Thorne [1] to smoothly match the inspiral phase onto the transition to plunge. In the spirit of the "numerical kludge waveform", we derive an approximate waveform from this transition trajectory using a flat–spacetime emission formulae applied to the transition orbit and plunge geodesic given by the transition model [15]. The inspiral waveform includes the dominant modes $\ell = m = 2$, $\ell = -m = 2$ only and so, for consistency, we included only the same two dominant modes in the expressions for the waveform during the merger phase.

The second model, used for non–spinning black holes, uses the EOB prescription [16, 17] to describe the plunge and merger phases. The EOB model is a framework in which the motion of a binary is represented as the effective motion of a test object in a background. Although we use the EOB model only in the non-spinning limit, an extension of the EOB scheme does exist which includes leading–order spin–orbit and spin–spin dynamical effects of a binary system for an "effective test particle" moving in a Kerr–type metric [22], and next–to–leading–order spin–orbit couplings [23]. However, it has been recently found [24] that it is not straightforward to include higher–order non–spinning PN couplings, such as the 4PN and 5PN adjustable parameters that were recently calibrated to numerical relativity simulations for non-spinning systems [25, 26], using these Hamiltonians [22, 23]. Additionally, the EOB Hamiltonian in [23] does not reduce to the Hamiltonian of a spinning test particle in Kerr spacetime. This issue was recently resolved in [27], in which a canonical Hamiltonian was derived for a spinning test particle in a generic curved spacetime at linear order in the particle spin. The construction of an improved EOB Hamiltonian based on the results of [27] is currently under development [24]. The Hamiltonian derived in [23] has recently been used in an exploratory study to calibrate the EOB parameters using numerical relativity simulations of spinning, non–precessing, equal mass BHs. This is the same approach that was previously used with great success for non-spinning black hole systems, e.g., to derive fits for the final mass and spin of a BH after merger that are consistent with NR to about $\sim 2\%$ accuracy [28]. We used the non-spinning EOB model only in this work because that model is more mature. However, the EOB model has recently been used to model circular–equatorial extreme–mass–ratio inspirals (EMRIs) around spinning supermassive black holes, using fits of various post–Newtonian parameters to Teukolsky–based waveforms [29]. Comparisons between an IMRI model based on this spinning EOB framework and the waveforms constructed using the transition model should be pursued in the future.

The final ingredient, again common to both models, is the ringdown waveform. This originates from the distorted Kerr black hole formed after merger, and consists of a superposition of quasinormal modes (QNMs). Each mode has a complex frequency, whose real part is the oscillatory frequency, and whose imaginary part is the inverse of the damping time. Following Berti, et. al. [30], and Buonanno, et. al. [31], we developed a RD model that includes the fundamental mode ($\ell = 2, m = 2, n = 0$) and two overtones ($n = 1, 2$). QNMs always come in "pairs". In general, a mode with a given (ℓ, m) will always contain a superposition of two different damped exponentials [30], one with positive real part of the frequency, and the other with negative real part of the frequency and different damping time, the so–called, "twin modes". Omitting these modes would have no serious consequences for non–rotating black holes, but it is conceptually inconsistent for rotating black holes. Furthermore, a single–mode expansion restricts attention to circularly polarized gravitational waves. We have not overlooked these problems and have modelled the RD phase with a general superposition of modes. On the other hand, to uniquely determine the frequencies and damping times of the newly formed Kerr BH after merger, we used fits for the final mass and spin found in [16, 32]. The various QNMs are attached to the plunge and merger waveform by imposing the continuity of the waveform and all necessary higher order time derivatives.

Part of the motivation in developing a waveform model using the transition model of Ori & Thorne is to enable a more straightforward extension of this present waveform model for circular–equatorial IMRIs to a waveform model for generic (eccentric–inclined) IMRIs. The "numerical kludge" inspiral waveform [21] and the transition model [33] are both already available for generic orbits. The mass–ratio regime that we explore in these papers has not been as exhaustively explored as the comparable–mass–ratio and extreme–mass–ratio regimes. While the present paper was being prepared, results of a numerical simulation were published which shed light on the gravitational energy and momenta radiated by BH binaries with mass–ratios 100:1 [34]. However, this was the first numerical simulation in the IMRI regime. The schemes described here combine elements of comparable mass and extreme-mass-ratio models in a logical way, but it cannot presently be tested against accurate simulations. As numerical and analytic models improve, these models should be refined. Nonetheless, the models should capture the main features of real IMRI waveforms and thus should be adequate for our purposes, namely to scope out the parameter estimation accuracies that might be achievable with ET. By using two alternative models we can build up further confidence in the results. In [15] we compared the two waveform models for non–spinning systems and demonstrated that the waveforms agreed well in both phase and amplitude, with differences at the level of a few percent. We show sample waveforms computed using the two models in Figure 2. The close agreement for non-spinning systems is clear from the figure in the lower panel. In this paper, we will now use these models to estimate the precision with which different third-generation detector networks will be able to estimate the parameters of the various binary systems described above.

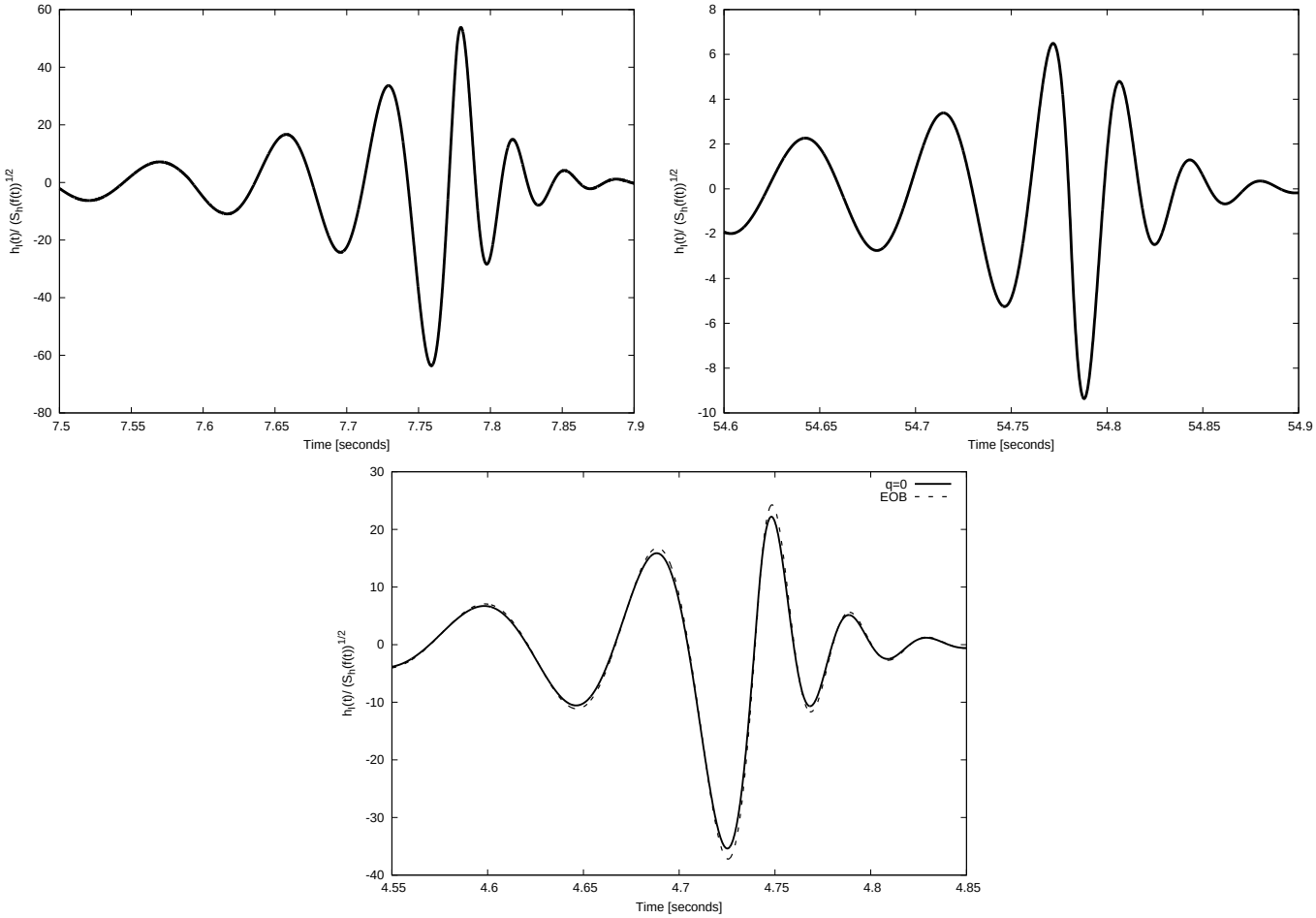

FIG. 2: We show complete gravitational waveforms for compact objects of masses $10\,M_\odot$ —top left panel, and $1.4M_\odot$ —top right panel, orbiting around a $500M_\odot$ BH with spin parameter $q = 0.3$. The bottom panel shows gravitational waveforms for a binary system consisting of a compact object of mass $10\,M_\odot$ and an IMBH of mass $500M_\odot$, computed using both the EOB and transition models. In each case, the various extrinsic parameters were chosen randomly.

IV. SIGNAL ANALYSIS

In this section we will briefly review the aspects of signal analysis relevant to our calculations. A GW detector is a linear system whose input is a GW we want to detect and whose output is a time series, which is a combination of both GW signals and instrumental noise. As mentioned above, any number of coplanar and colocated detectors have a response to GWs that can be written as a linear combination of the responses of two right–angle detectors offset by 45°. The output of these two equivalent two arm Michelson detectors can be represented as

$$s_\alpha(t) = h_\alpha(t) + n_\alpha(t), \qquad \alpha = \mathrm{I},\ \mathrm{II}, \tag{3}$$

where I, II denote the data streams from the two detectors. The detection problem is to distinguish $h_\alpha(t)$ from $n_\alpha(t)$. With the assumptions that (a) each Fourier component of the noise $\tilde{n}_\alpha(f)$ has a Gaussian probability distribution; and (b) the noise is stationary, i.e., the different Fourier components are uncorrelated, the ensemble average of the Fourier components of the noise have the property

$$\langle \tilde{n}_\alpha(f)\, \tilde{n}_\beta(f')^* \rangle = \frac{1}{2}\delta(f - f')S_n(f)\delta_{\alpha\beta}. \tag{4}$$

This relation defines the one-sided spectral density of the instrumental noise, $S_n(f)$.

We wish to estimate the parameters of a system from which we have detected gravitational waves. If the expected waveform $h(t;\theta)$ depends on parameters $\theta = \{\theta_1, ..., \theta_N\}$, we want to construct the posterior probability of the

parameters given the data and from that we will find the most probable value of the parameters of the source and their respective errors.

There is a natural inner product on the vector space of signals, which for any two signals $p_\alpha(t), q_\alpha(t)$, takes the form

$$(\mathbf{p}\,|\,\mathbf{q}) \equiv 2\sum_\alpha \int_0^\infty \left[\frac{\tilde{p}^*_\alpha(f)\tilde{q}_\alpha(f) + \tilde{p}_\alpha(f)\tilde{q}^*_\alpha(f)}{S_n(f)}\right] \mathrm{d}f. \tag{5}$$

The probability distribution for Gaussian noise, $n(t)$, is given by

$$p(\mathbf{n}_0) = N\exp\left(-\frac{(\mathbf{n}_0\,|\,\mathbf{n}_0)}{2}\right), \tag{6}$$

where N is a normalization factor. This relation gives the probability that the actual noise realization is $\mathbf{n_0}$. If the source had parameters $\vec{\theta}$, the output would have the form $\mathbf{s}(t) = \mathbf{h}(t;\vec{\theta}) + \mathbf{n}_0(t)$. Using this relation and Equation (6), we obtain the likelihood of observing the output $s(t)$ if the signal had parameters $\vec{\theta}$

$$\Lambda\left(\mathbf{s}|\vec{\theta}\right) = N\exp\left(-\frac{\left(\mathbf{s}_0 - \mathbf{h}(\vec{\theta})\,|\,\mathbf{s}_0 - \mathbf{h}(\vec{\theta})\right)}{2}\right). \tag{7}$$

We can re–write Eq. (7) using Bayes' theorem, which states that the posterior probability is proportional to the product of the likelihood function and the prior probability. The prior describes the degree of belief that a GW signal in the data would have parameters $\vec{\theta}$ in the data before the measurement is made, and the posterior probability describes the degree of belief after. Denoting the prior by $p_0(\vec{\theta})$, the posterior probability for the parameters $\vec{\theta}$, given the observed output s, is given by [35]

$$p\left(\mathbf{h}(\vec{\theta})\,|\,\mathbf{s}\right) \propto p_0(\vec{\theta})\exp\left(\left(\mathbf{h}(\vec{\theta})\,|\,\mathbf{s}\right) - \frac{1}{2}\left(\mathbf{h}(\vec{\theta})\,|\,\mathbf{h}(\vec{\theta})\right)\right). \tag{8}$$

As $p\left(\mathbf{h}(\vec{\theta})\,|\,\mathbf{s}\right)$ is a distribution in $\vec{\theta}$ for a fixed output $\mathbf{s}$, the term $(\mathbf{s}\,|\,\mathbf{s})/2$ can be absorbed into the normalization factor. This probability distribution function describes the information we can extract from the data stream once the prior is given.

In the absence of an actual data set, we cannot compute this posterior probability distribution, but we can estimate how broad the posterior will be and hence how well we might constrain the parameters. Assuming a flat prior (or a locally-flat prior which would be a reasonable assumption for a signal of high signal-to-noise ratio), the maximum posterior probability is the maximum-likelihood value, which minimizes $(\mathbf{s}-\mathbf{h}\,|\,\mathbf{s}-\mathbf{h})$. This is also the point in parameter space with the highest matched filtering signal–to–noise ratio (SNR)

$$\frac{S}{N}[h(\theta^i)] = \frac{(\mathbf{s}\,|\,\mathbf{h})}{\sqrt{(\mathbf{h}\,|\,\mathbf{h})}}. \tag{9}$$

We can expand Eq. (8) about this peak, $\hat{\theta}$ by setting $\theta^i = \hat{\theta}^i + \Delta\theta^i$ to obtain

$$p(\Delta\theta\,|\,s) \approx \mathcal{N}\, e^{-\frac{1}{2}\Gamma_{ij}\Delta\theta^i\Delta\theta^j}, \qquad \Gamma_{ij} \equiv \left(\frac{\partial\mathbf{h}}{\partial\theta^i}\,\middle|\,\frac{\partial\mathbf{h}}{\partial\theta^j}\right)_{|\theta=\hat{\theta}}. \tag{10}$$

Γ_{ij} is the Fisher Information Matrix. This approximation is valid for large SNR. The correlation matrix of the errors $\Delta\theta^i$ is given by

$$\left\langle \Delta\theta^i\Delta\theta^j \right\rangle = (\Gamma^{-1})^{ij}. \tag{11}$$

We shall make use of Eq. 11 to estimate parameter errors for the various binaries described in Section II B. For white noise, i.e., $S_n(f) = \text{const.}$, Parseval's theorem allows us to rewrite the inner product (5) in the simple form [36]

$$2\frac{1}{S_n}\sum_\alpha \int_{-\infty}^{\infty} p_\alpha(t)q_\alpha(t)dt. \tag{12}$$

We can use this definition of the inner product to simplify our analysis. If we define the "noise–weighted" waveform

$$\hat{h}_\alpha(t) \equiv \frac{h_\alpha(t)}{\sqrt{S_h\big(f(t)\big)}}, \qquad f(t) = \frac{1}{\pi}\frac{\mathrm{d}\phi}{\mathrm{d}t}, \tag{13}$$

we can then rewrite the Fisher matrix approximately as [36]

$$\Gamma_{ab} = 2\sum_\alpha \int_0^T \partial_a \hat{h}_\alpha(t)\partial_b \hat{h}_\alpha(t)\mathrm{d}t\,, \qquad \text{where } \partial_a \equiv \partial/\partial\theta^a. \tag{14}$$

As discussed in [15], the binaries we shall consider have relatively low SNR and it is known that in such situations the Fisher Matrix may overestimate measurement accuracies. Vallisneri [37] gave a mismatch criterion to determine whether Fisher Matrix results were reliable in a particular context. This idea is to compute the ratio $r(\theta, \mathrm{A})$ of the linearized signal amplitude (LSA) likelihood to the exact likelihood. This ratio r is given by [37]

$$|\log r(\theta, \mathrm{A})| = (\Delta\theta_j h_j - \Delta h(\theta), \Delta\theta_k h_k - \Delta h(\theta))\,, \tag{15}$$

where A represents the signal strength, $\Delta h(\theta) = h(\theta) - h(\hat{\theta})$, with $\theta = \hat{\theta} + \Delta\theta$, and $\hat{\theta}$ the observed location of maximum LSA likelihood for a given experiment. We use the consistency criterion, Eq. (15), to explore the 1–σ likelihood surface predicted by the Fisher Matrix to verify that the mismatch between the LSA and the exact likelihoods is small. Ratios below a fiducial value, say $|\log r(\theta, \mathrm{A})| \sim 0.1$, are considered acceptable [37].

As an example of typical results obtained from this analysis, for $(10M_\odot, 100M_\odot)$ binaries with $q = 0.3$, we found that systems near the lower quartile of the distribution had $|\log r(\theta, \mathrm{A})| \sim 0.2$. From this threshold onwards, the ratio r decreases gradually so that at the upper quartile of the distribution we obtain $|\log r(\theta, \mathrm{A})| \sim 0.04$. This indicates that the results we get from the Fisher Matrix should be a reasonable estimate of the measurement precisions achievable for IMRIs using ET. Our results may be somewhat optimistic and at some point should be verified using Monte Carlo simulations to recover the full posterior probability distributions. Such an exercise is beyond the scope of this present work. Nonetheless, the results should be fairly accurate, and we will see in Section V that, for parameters which can be compared, these results are in good accord with previous results that have been derived for other types of binary and different waveform models.

The Fisher matrix for a network of detectors is given by the sum of the individual Fisher Matrices for each detector. When modelling the response of the various detectors, it is necessary to account for their relative positions on the surface of the Earth, as the corresponding time delays are what allow source triangulation. In computing the waveforms used in the Fisher Matrix, we found it convenient to use two different timesteps in order to separately resolve the (slow) inspiral and (fast) merger/ringdown phases. We checked that varying the choice of timesteps and the location of the transition between the two timesteps did not significantly affect the results for any of the systems considered. We will discuss the convergence of the Fisher Matrix scheme further in Section V.

V. PARAMETER ESTIMATION ERROR RESULTS

The parameter space of the signals we shall consider is 10 dimensional. Four of these are intrinsic parameters, namely $\ln m, \ln M, q, t_0$. The other six are extrinsic parameters. We summarize the physical meaning of all the parameters in Table I.

To explore parameter estimation errors using the inverse Fisher Matrix we fix the values of the intrinsic parameters of the source, and carry out a Monte Carlo over possible values for the extrinsic parameters. The parameter error scales with the SNR of the source as 1/SNR, so we quote results at a fixed SNR=30. To do this, we first compute the Fisher Matrix for a source at a fixed distance, $D = 6.6348$Gpc, and obtain the SNR at that distance from the expression

$$\mathrm{SNR}^2 = 2\sum_{\alpha=I,II}\int_{t_{\rm init}}^{t_{\rm LSO}} \hat{h}_\alpha^2(t)dt. \tag{16}$$

We then multiply the errors estimated from the Fisher Matrix by (SNR/30) to normalise an SNR of 30. The observation time starts when the GWs from the inspiral reach a frequency of 5Hz and finishes when the RD waveform is no longer contributing to the SNR.

$\ln m$	mass of compact object (CO)
$\ln M$	mass of SMBH
q	magnitude of (specific) spin angular momentum of SMBH
t_0	time at which orbital frequency sweeps through a reference value
ϕ_0	Initial phase of CO orbit
θ_S	source sky colatitude in an ecliptic–based system
ϕ_S	source sky azimuth in an ecliptic–based system
θ_K	direction of SMBH spin (colatitude)
ϕ_K	direction of SMBH spin (azimuth)
$\ln D$	distance to source

TABLE I: This table shows the physical meaning of the parameters used in our model. The angles (θ_S, ϕ_S) and (θ_K, ϕ_K) are defined in a fixed ecliptic–based coordinate system.

A. Dependence of parameter estimation errors on system parameters

We consider the twelve different binary systems described in Section II B. For the sources with $q = 0.3$, 0.9 we present results computed from the transition model for the waveform. For the non-spinning systems, $q = 0$, we present results from both the transition model and the EOB model. The Tables II–V list the mean, standard deviation, median and lower and upper quartiles of the distribution of the log to base 10 of the Fisher Matrix errors computed in the Monte Carlo simulation. There is one table for each of the four mass combinations we consider. These results assume the optimistic 3 ET network configuration, and hence should be considered as upper bounds on the accuracy with which we may be able to measure the various parameters.

In Figure 5 we show histograms of the error estimates for several parameters found in the Monte Carlo simulation for the $m = 10M_\odot$, $M = 100M_\odot$, $q = 0.9$ system. This figure, and Table II, indicate that a network of 3 ETs might be able to determine the location of the source in the sky to an accuracy of $\sim 10^{-3}$ steradians, i.e., ~ 4 square degrees. This estimate is the statistical mean of the Monte Carlo distribution at SNR of 30 assuming the optimistic detector network of three ETs in the geographic locations of Virgo, LIGO Livingstone and Perth, Australia (AIGO). Recent work has shown that for the existing LIGO-Virgo detector network, assuming uniform distribution of sources, at an optimal network SNR of around 15, 50% of inspiral sources can be located within 23 sq–degs (best case) at the 95% confidence level. For burst sources, without any knowledge of the waveform, 50% of the sources can be localized within 50 sq–degs (worst case) at an SNR of 10, but this can be reduced to 8 sq–degs if predicted waveforms are available [38]. These estimates are similar for the initial or advanced detectors [38], at a fixed SNR. The inclusion of an additional detector in the Southern Hemisphere, such as AIGO, can further improve these values as it contributes a longer baseline, additional energy flux, extended signal space, and breaks the plane–degeneracy formed by the three detector network of LIGO Livingstone, LIGO Hanford and Virgo [38]. Just before submitting this paper, [39] presented results for the accuracy with which sources can be localized with a network of GW detectors, using only timing information in the various detectors. Fainhurst [39] has found that increasing the number of detectors at different sites increases both the absolute number of observable sources, and greatly increases the fraction of sources that can be well localized. For instance, at fixed SNR of 8, and using the advanced detector network comprising the two LIGO detectors at Hanford (HH) and LIGO Livingstone (L), no sources can be localized within 20 sq–degs. Adding another detector at a different site, e.g., a LIGO detector in Australia (A), or advanced Virgo (V), or the Japane LCGT detector (J), the networks HLA, HHLV, HHJL, can localize up to 50% of the signals within 20 sq–degs, and the loudest signals within 5 sq–degs. In all these results, it was found that for the networks involving an Australian detector, the peak of the localization distributions takes place between 5 and 10 sq–degs. Our results imply that we can determine the location of the source in the sky to an accuracy of ~ 12 sq–degs at an SNR of 8, and this estimate is the statistical median value found in the Monte Carlo simulation. Our results are therefore in good accord with existing estimates of the angular resolution that could be achieved by the advanced detector network. Furthermore, Table II shows that in the non–spinning limit, we can resolve the plunge time t_0 to within ~ 22 ms at SNR of 10. This estimate is also in good accord with the results obtained independently by Ajith et al. [40] and Luna et al. [41].

The Monte Carlo simulations also show that we expect to determine the total mass of $m = 10M_\odot\,, M = 100M_\odot$ binaries to an accuracy of $\sim 0.1\%$ in the non–spinning limit at SNR of 8. This predicted accuracy is in good accord with previous estimates for related systems. In [42] it was estimated that using exactly the same 3ET detector network that we have considered in this paper, we would be able to determine the total mass of $m = 23M_\odot\,, M = 100M_\odot$ binaries with mass ratio $\eta = 0.16$, to an accuracy of $\sim 0.1\%$ in the non–spinning limit at a network SNR of 8. This estimate was obtained using the phenomenological waveform model described in [43], which includes the inspiral,

merger and ringdown for non–spinning binaries of comparable mass in a consistent way. Figure 3 shows the accuracy with which we expect to determine the masses of the small CO and the IMBH for spinning systems, as well as the IMBH's spin parameter q.

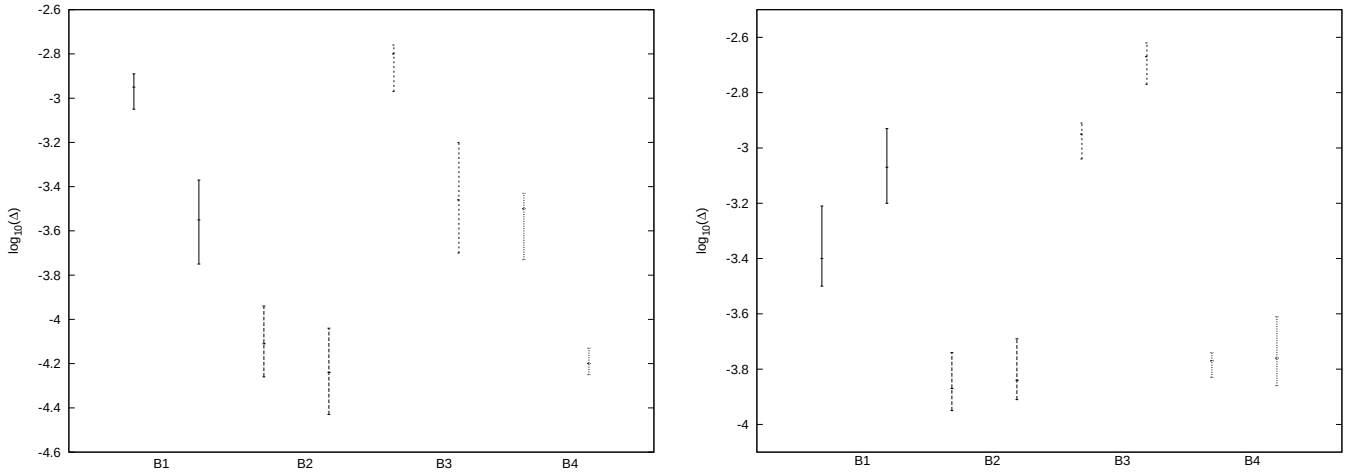

FIG. 3: Left panel: expected errors in the masses of the small CO and the IMBH for a fixed value of the IMBH's spin parameter $q = 0.3$. There is a pair of candlesticks for each of the four binary systems. For each binary, the candlestick representing the CO's mass error estimate is to the left of that for the IMBH's mass error estimate. Notice that the errors are reported as the logarithm to base ten $\log_{10}(\Delta)$ on the vertical axis. The error bars indicate the lower and upper quartiles found in the Monte Carlo simulation. Right panel: expected errors in the IMBH's spin parameter for two different values for the spin parameter q. For each system, the candlestick corresponding to a central IMBH with $q = 0.3$ is to the right of that associated with the error estimate for a system with $q = 0.9$. The continuous, long–dashed, dashed and dotted lines represent systems B1: $m = 10M_\odot\,, M = 100M_\odot$, B2: $m = 1.4M_\odot\,, M = 100M_\odot$, B3: $m = 10M_\odot\,, M = 500M_\odot$, and B4: $m = 1.4M_\odot\,, M = 500M_\odot$, respectively.

Figure 3 shows that for binaries that stay the longest in band, namely the $m = 1.4M_\odot\,, M = 100M_\odot$, $q = 0.3$ system (~ 291 seconds in band), we can determine the masses of the CO and the IMBH to an accuracy of 0.01%, 0.005%, respectively, at an SNR of 30. The accuracy gradually decreases for the shorter–lived events. For instance, for binaries with $m = 10M_\odot\,, M = 500M_\odot$, $q = 0.3$, which stay in band about ~ 8.3 seconds, we expect to measure the CO's and IMBH's masses to an accuracy of $\sim 0.15\%$, $\sim 0.05\%$, respectively, at an SNR of 30.

We expect to determine the spin parameter more accurately for rapidly rotating binaries. For instance, the estimated accuracy with which we can measure the IMBH's spin for binaries with $m = 10M_\odot\,, M = 100M_\odot$, $q = 0.9$ is $\sim 0.05\%$. This is about a factor of 2 better than for binaries with the same component masses but with spin $q = 0.3$. We would expect this trend since, for more rapidly spinning systems, the small CO comes much closer to the outer horizon of the Kerr IMBH before merging, and this is the regime where the CO can more strongly feel the effects of the IMBH's spin.

In general, we expect that the precision with which we can measure the parameters of a binary depends on the number of GW cycles that are observed. Therefore, we might expect the precision to depend on the source masses as, from best to worst, $1.4M_\odot + 100M_\odot$, $1.4M_\odot + 500M_\odot$, $10M_\odot + 100M_\odot$, $10M_\odot + 500M_\odot$. Tables II–V, and Figure 3 confirm this expectation. These Tables also show that the precision improves for more rapidly spinning IMBHs. This is because, for greater spins, the inspiral phase evolution lasts longer and so there are more cycles of information in the waveform. The SNR of the spinning systems will also be larger at a given distance, as compared with slowly spinning IMBHs, so these systems can be seen further away. This does not affect the results quoted here, which are normalised to fixed SNR=30. Tables II–V also confirm that our two independent waveform models make predictions for the parameter estimation errors for non-spinning systems that are consistent to better than ten per cent.

Finally, we note that the consistency of the distributions of Figure 5, in the sense that they are smooth with few outliers, is an indication that the results are convergent. It is well known that Fisher Matrices encountered in parameter estimation calculations for GW sources can have very large condition numbers. However, the results we shall present here were obtained from Fisher Matrices that exhibited convergence over at least two orders of magnitude in the offsets used to compute the numerical waveform derivatives. The inverse matrices were computed using an LU decomposition, and we verified that the Inverse Fisher matrices were also convergent to $\lesssim 10\%$ over an order of magnitude in the numerical offsets. We also found that the offsets required for the various network configurations were consistent, as we would expect, since the convergence of the FM should depend on the intrinsic waveform, rather

than the choice of network.

B. Dependence of parameter estimation errors on network configuration

We shall now consider the more modest network configurations C1–C4 described earlier, which consist of combinations of ET's and right–angle detectors at 2 or 3 sites from Virgo, LIGO Livingstone and Perth. These results are shown in Tables VI–IX[1] for the four different mass combinations, but with the central IMBH spin fixed at $q = 0.3$. As expected, we find that a single ET is sufficient for accurate intrinsic parameter determination. This is because the signature of the intrinsic parameters is encoded in the phase evolution. Having normalised intrinsic parameter errors to a fixed network SNR of 30, Figure 4 shows clearly that the accuracy with which we can measure the intrinsic parameters of a binary is not dramatically increased as a function of the network configuration.

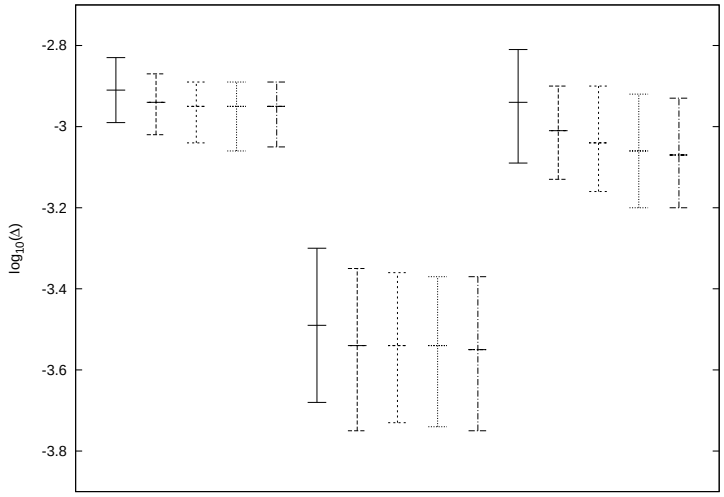

FIG. 4: Arranged from left to right in the panel, we show expected errors in the CO's mass, IMBH mass and IMBH spin parameter, as a function of the network configuration for binary systems with $10M_\odot + 100M_\odot$ and IMBH's spin $q = 0.3$. In each group the candlesticks are arranged in order C1–C5 from left to right.

However, it is not possible to constrain the location of the source in the sky nor the luminosity distance using a single detector. This is also expected, as the determination of the extrinsic parameters comes from the time–delays between different detectors. It appears that the inclusion of an additional right–angle detector (configuration C2) is enough to constrain the source sky position and luminosity distance to moderate precision ~ 30 sq–degs, $\sim 15\%$ for a $10M_\odot$ BH IMRI into a $100M_\odot$ IMBH with spin $q = 0.3$ at SNR of 30. Replacing this right–angle detector by another ET at the same location (configuration C3) enhances the determination of these parameters to ~ 12 sq–degs, $\sim 10\%$, respectively. If we consider a configuration consisting of 1 ET, plus two right–angle detectors (configuration C4) these estimates are further improved to ~ 11 sq–degs, $\sim 10\%$, respectively. These two estimates are rather close to the precision we expect to obtain using a 3 ET network, namely, ~ 8 sq–degs, $\sim 10\%$, respectively. These results also show that the distributions become narrower for the more complex configurations, i.e., there is less variation in the precisions with which we can determine the extrinsic parameters as we randomise over the source position and orientation. This is also expected, as a more complex network should provide more complete sky coverage. We can compare our results for the luminosity distance in the non–spinning limit with those quoted in Table I of [42], which were quoted at a network SNR of 8. For non–spinning systems and assuming network C1, we find that we can estimate the luminosity distance to an accuracy of $\sim 40\%$ at an SNR of 8. Using configuration C2, we can determine the luminosity distance to an accuracy of 30% and for C3, the estimate improves marginally to $\sim 28\%$. This estimate is roughly the same for a 3ET detector network. Hence, we conclude that using 1 ET plus one right-angle detector would be enough to constrain the luminosity distance to within $\lesssim 40\%$ at an SNR of 8. These estimates are in good

[1] Note that only Table VI is included in the main text. Tables VII–IX have been moved to Appendix A to prevent an overload of information.

accord with Table I of [42], which were computed for comparable-mass systems using an inspiral-merger-ringdown waveform model. This comparison illustrates again that even if the IMRI models used in this paper are not accurate enough to be used for detection of IMRI systems, they do still capture the main features of the systems with sufficient accuracy that they can be used for parameter estimation studies and to illustrate the potential scientific impact of the ET.

In summary, a single ET will be enough to measure the intrinsic parameters but will not be sufficient to accurately reconstruct the extrinsic parameters. Extrinsic parameter determination is possible with the addition of one right-angle detector, but a 2 ET configuration will improve the accuracy with which we can measure the source's sky position and luminosity by roughly a factor of ~ 2. A more optimistic configuration consisting of a single ET and two right-angle detectors upgraded to ET's sensitivity will generate results that are competitive with the highly optimistic three ET network. This configuration (C3) might be more realistic, since it will have lower overall costs, although it is not simply an upgrade of existing sites as we are assuming 10km scale right-angle interferometers.

Tables II–IX show that GW observations will produce valuable astrophysical results. A network of 2 ETs operating in coincidence will be able to measure accurately the masses of two merging black holes and the luminosity distance at which such an event is taking place. If we see light black holes at high redshift this is important for constraining models of the early growth of structure. To identify mergers between seed black holes, we need to be able to find out whether the mass is low, $M \lesssim 10^3 M_\odot$, and the redshift is high, $z \gtrsim 3$. As discussed in [42], we can translate the luminosity distance estimate into a redshift estimate, which gives the redshift to a similar precision as the distance. In paper I of this series we estimated that we could potentially detect hundreds of BHs of mass $\sim 16 M_\odot$, $\sim 100 M_\odot$, up to redshifts of $z \sim 5$, $z \sim 4$, if such systems exist. The parameter estimation results suggest that we should be able to confidently say that any events with $M \sim 100 M_\odot$ and $z \sim 5$ that are detected are indeed mergers between *light* black holes occurring at *high* redshift [42]. As mergers between $\sim 100 M_\odot$ seed black holes generate GWs in the 0.1Hz–10Hz band, ET will be the first detector able to probe such systems. It could therefore play a fundamental role in probing the hierarchical assembly of structure in the Universe by detecting the first epoch of mergers and probing the mass distributions of seeds. By contrast, LISA will primarily detect subsequent mergers between more massive black holes that have grown from these seeds. In this sense, ET will provide complementary observations to LISA. Future missions like the space–based detector DECIGO will perform a complete survey of MBHB mergers taking place during its lifetime. It is not inconceivable that DECIGO will operate concurrently with ET, allowing simultaneous observations. If DECIGO flies after ET, then the detections it makes will confirm the earlier results of ET and LISA. In summary, the information provided by these GW detectors will be essential to falsify the standard cosmological models for galaxy formation and growth, and to constrain the heavy–seed model. Another particularly promising possibility for GW astronomy is the detection of IMBHs in globular clusters. With regard to black hole formation in these environments, it is expected that a fraction $\sim 10^{-6}$ to 10^{-4} of the $\sim 10^6$ initial stars will become stellar–mass BHs via normal stellar evolution [44]. All these BHs should have formed before ~ 10 Myr, with the most massive BHs forming at around ~ 3 Myr [45]. These black holes should be more centrally concentrated that main sequence (MS) stars for various reasons, namely, significant mass segregation of the initial, higher mass progenitor [46], preferential formation of stars near the cluster centre [47], and because BH birth kicks are not expected to displace BHs into the cluster halo [48]. Even if we assume that the BHs were distributed throughout the cluster, mass segregation should be able to assemble a subcluster of BHs near the centre after at most ~ 100 Myr, assuming a typical cluster with relaxation time of 1 Gyr [49]. During mass segregation, BH–MS binaries will undergo three body and four body interactions that will replace the MS star by a heavier BH. Simulations conducted by [49, 50] suggest that, whether formed through successive BH mergers or stellar collisions, it is more likely to find an IMBH in clusters with dense cores, i.e., IMBHs may exist in some tens of percent of current globulars. In this type of clusters, the first formation of IMBHs with mass $\sim 100 M_\odot$ occurs at ~ 10 Myr after the subcluster of BHs is formed. BHs may stay in the cluster, and not be ejected by hardening and eventual recoil, by means of the Kozai mechanism in stable hierarchical triples. With regard to BH–BH mergers, these can occur only through GW emission in binaries, possibly enhanced by dynamical interactions in the cluster. This is so because BHs have negligible cross sections for direct collisions. A combination of these various mechanisms, e.g., secular Kozai resonance, binary exchange processes, gravitational radiation, three and four–body interactions, may drive the merger of these IMBHs and lower–mass COs, and in turn, increase the likelihood that IMRIs in globular clusters will be detectable by their gravitational radiation by ground–based laser interferometers [10]. As discussed in this paper, these GW observations will provide rigorous measurements of the masses of IMBHs and, hopefully, will allow direct evidence, beyond doubt, for their existence [9].

The Monte Carlo results we present in this paper are the first results for IMRI source detectable by ET to appear in the literature. The results must be taken with some caution, because of the approximations in the waveform models that have been made, as discussed earlier. However, these results should accurately reflect the likely order-of-magnitude of the parameter measurement errors that could be achievable. The precise astrophysical implications will depend primarily on the number of events that are seen, which is very difficult to predict given the existing

uncertainties in the astrophysics of IMBHs.

Model		Statistics of distribution of $\log_{10}(\Delta X)$ for error, ΔX, in parameter $X =$									
		$\ln(m)$	$\ln(M)$	q	t_0	ϕ_0	θ_S	ϕ_S	θ_K	ϕ_K	$\ln(D)$
q=0.9	Mean	-3.13	-3.60	-3.43	-1.73	-0.59	-1.39	-1.26	-1.01	-0.91	-0.94
	St. Dev.	0.192	0.329	0.446	0.355	0.133	0.164	0.268	0.526	0.553	0.397
	L.Qt.	-3.19	-3.74	-3.50	-1.85	-0.63	-1.52	-1.46	-1.36	-1.30	-1.25
	Med.	-3.09	-3.57	-3.40	-1.69	-0.54	-1.38	-1.29	-1.19	-1.06	-1.06
	U. Qt.	-3.01	-3.41	-3.21	-1.52	-0.50	-1.26	-1.11	-0.81	-0.65	-0.68
C5	Mean	-3.03	-3.57	-3.11	-1.82	-0.67	-1.38	-1.25	-0.99	-0.86	-0.87
	St. Dev.	0.279	0.320	0.203	0.331	0.232	0.207	0.270	0.591	0.656	0.479
	L.Qt.	-3.05	-3.75	-3.20	-1.95	-0.70	-1.53	-1.45	-1.38	-1.31	-1.24
	Med.	-2.95	-3.55	-3.07	-1.78	-0.62	-1.38	-1.28	-1.20	-1.05	-1.00
	U. Qt.	-2.89	-3.37	-2.93	-1.63	-0.57	-1.25	-1.11	-0.78	-0.58	-0.63
q=0	Mean	-3.35	-3.64	N/A	-1.85	-0.79	-1.37	-1.24	-0.97	-0.84	-0.86
	St. Dev.	0.553	0.435	N/A	0.412	0.306	0.200	0.272	0.573	0.604	0.448
	L.Qt.	-3.33	-3.77	N/A	-2.03	-0.80	-1.51	-1.45	-1.35	-1.28	-1.22
	Med.	-3.31	-3.60	N/A	-1.88	-0.73	-1.37	-1.27	-1.16	-1.03	-0.98
	U. Qt.	-3.17	-3.41	N/A	-1.77	-0.68	-1.25	-1.09	-0.71	-0.53	-0.57
EOB	Mean	-3.55	-3.68	N/A	-1.94	-0.91	-1.39	-1.27	-1.02	-0.89	-0.91
	St. Dev.	0.229	0.195	N/A	0.224	0.157	0.174	0.244	0.598	0.631	0.464
	L. Qt.	-3.71	-3.81	N/A	-2.14	-1.01	-1.53	-1.46	-1.38	-1.30	-1.26
	Med.	-3.53	-3.68	N/A	-1.97	-0.93	-1.39	-1.30	-1.21	-1.07	-1.04
	U. Qt.	-3.36	-3.54	N/A	-1.89	-0.80	-1.26	-1.13	-0.81	-0.68	-0.69

TABLE II: Summary of Monte Carlo results for parameter estimation errors. We show the mean, standard deviation, median and quartiles of the distribution of the logarithm to base ten of the error in each parameter. Results are given for a $m = 10M_\odot$ CO inspiralling into a $M = 100M_\odot$ IMBH for various choices of the IMBH spin, q, computed using the transition model waveform. We also show results for $q = 0$ computed using the EOB waveform model.

VI. CONCLUSIONS

In this paper, we have used the gravitational waveform models for IMRIs developed in paper I of this series [15] to estimate the precision with which the Einstein Telescope will be able to determine the parameters of circular–equatorial IMRIs. We have presented results for a set of twelve "typical" systems, comprising four different combinations of component masses — $1.4M_\odot + 100M_\odot$, $1.4M_\odot + 500M_\odot$, $10M_\odot + 100M_\odot$, and $10M_\odot + 500M_\odot$ — and three different IMBH spins — $q = 0, 0.3, 0.9$. For the non–spinning systems, we have compared the results from the transition model and the EOB waveform model and found that these models make predictions that are consistent to better than ten percent. This final check provides confidence in these results.

We have also explored how the accuracy of parameter determination depends on the configuration of the detector network using the "ET–B" noise curve and assuming a cut–off frequency of 5Hz. We have shown that a single ET is sufficient to accurately determine the intrinsic parameters of these systems. However, a network of detectors is required to obtain accurate estimates of the extrinsic parameters. A network of 2 ETs should be sufficient to measure the source's sky position and luminosity distance to accuracies of ~ 12 sq–degs and $\sim 10\%$, respectively, for a BH IMRI into a $100M_\odot$ IMBH with spin $q = 0.3$. A more sophisticated network comprising 1 ET and two right-angle detectors would have comparable precisions and these results are comparable to the precisions possible with a 3 ET network, which are ~ 8 sq–degs, 10%, respectively (at a source SNR of 30). Any of these ET networks would simultaneously constrain the BH and IMBH masses and the IMBH spin magnitude to fractional accuracies of $\sim 10^{-3}, 10^{-3.5}$ and10^{-3}, respectively. The amount of variation in the parameter precision over random choices of the source location and orientation also decreases for more complex network configurations. A 3 ET network is a highly optimistic assumption about a future third–generation GW detector network, but our results indicate that a more modest network comprising one ET and right-angle interferometers in LIGO Livingston and Perth can recover parameters to almost the same precision. This network would have lower associated costs and might therefore be more feasible. On the other hand, our results should be regarded as conservative, in the sense that using a lower

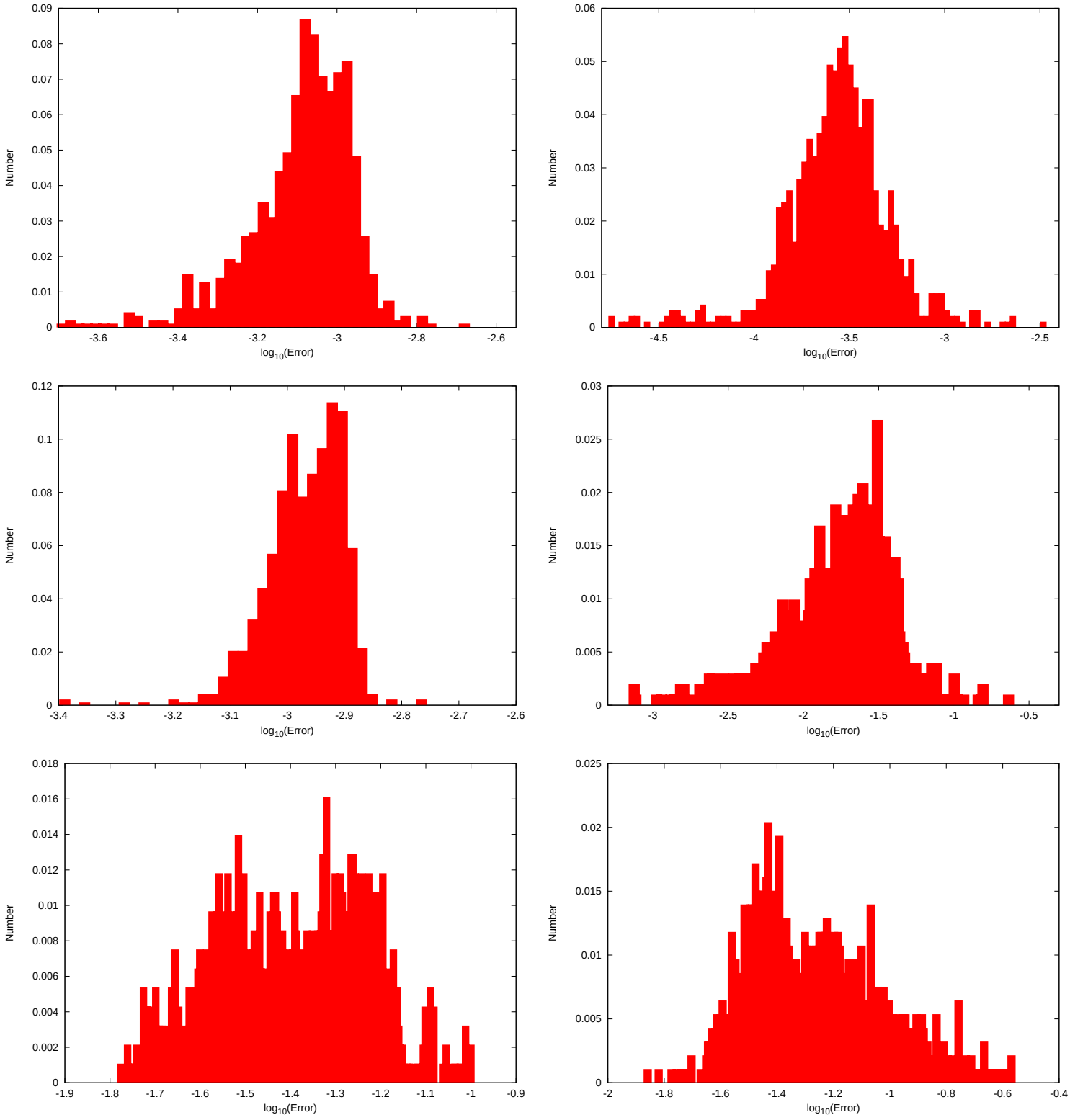

FIG. 5: Distribution of errors in various parameters computed in the Monte Carlo simulations. We show the system with $m = 10M_\odot$, $M = 100M_\odot$, $q = 0.9$. The panels show the error distributions in the following order, top row, from left to right, $\log_{10}(\Delta(\ln m))$, $\log_{10}(\Delta(\ln M))$; middle row, $\log_{10}(\Delta q)$, $\log_{10}(\Delta t_0)$; bottom row, $\log_{10}(\Delta\theta_S)$, $\log_{10}(\Delta\phi_S)$.

Model		Statistics of distribution of $\log_{10}(\Delta X)$ for error, ΔX, in parameter $X =$									
		$\ln(m)$	$\ln(M)$	q	t_0	ϕ_0	θ_S	ϕ_S	θ_K	ϕ_K	$\ln(D)$
q=0.9	Mean	-5.09	-5.39	-3.88	-1.71	-0.71	-1.40	-1.27	-0.91	-0.78	-0.91
	St. Dev.	0.261	0.271	0.318	0.333	0.262	0.163	0.260	0.599	0.616	0.461
	L.Qt.	-5.19	-5.49	-3.95	-1.88	-0.88	-1.53	-1.46	-1.32	-1.23	-1.27
	Med.	-5.05	-5.35	-3.87	-1.73	-0.82	-1.38	-1.31	-1.08	-0.91	-1.05
	U. Qt.	-4.93	-5.21	-3.74	-1.60	-0.51	-1.28	-1.14	-0.64	-0.48	-0.66
q=0.3	Mean	-4.09	-4.23	-3.87	-1.78	-0.73	-1.40	-1.29	-0.99	-0.86	-0.95
	St. Dev.	0.233	0.308	0.198	0.375	0.167	0.179	0.265	0.500	0.543	0.459
	L.Qt.	-4.26	-4.43	-3.91	-1.89	-0.83	-1.53	-1.47	-1.38	-1.30	-1.30
	Med.	-4.11	-4.24	-3.84	-1.77	-0.75	-1.38	-1.31	-1.21	-1.06	-1.14
	U. Qt.	-3.94	-4.04	-3.69	-1.68	-0.63	-1.27	-1.13	-0.75	-0.57	-0.73
q=0	Mean	-4.09	-4.22	N/A	-1.87	-0.78	-1.41	-1.29	-0.96	-0.85	-0.92
	St. Dev.	0.320	0.349	N/A	0.390	0.165	0.166	0.256	0.597	0.636	0.463
	L.Qt.	-4.33	-4.48	N/A	-2.03	-0.90	-1.52	-1.47	-1.36	-1.30	-1.28
	Med.	-4.17	-4.28	N/A	-1.89	-0.81	-1.39	-1.33	-1.15	-1.02	-1.07
	U. Qt.	-3.94	-3.99	N/A	-1.75	-0.67	-1.28	-1.15	-0.74	-0.58	-0.68
EOB	Mean	-4.06	-4.20	N/A	-1.92	-0.79	-1.39	-1.28	-0.97	-0.84	-0.89
	St. Dev.	0.130	0.189	N/A	0.197	0.091	0.166	0.261	0.648	0.678	0.496
	L.Qt.	-4.15	-4.38	N/A	-1.96	-0.84	-1.52	-1.47	-1.37	-1.28	-1.25
	Med.	-4.07	-4.22	N/A	-1.90	-0.78	-1.38	-1.32	-1.20	-1.05	-1.05
	U. Qt.	-3.97	-4.09	N/A	-1.86	-0.74	-1.26	-1.14	-0.78	-0.60	-0.66

TABLE III: As Table II, but now for binary systems with a CO of mass $m = 1.4M_\odot$.

cut–off frequency or asumming a different ET design, e.g., the xylophone configuration, [2] may improve the various results quoted in these papers. At present we have made use of the official "ET–B" noise curve [18], but a study of the potential applications of ET using both lower cut–off frequencies and more optimistics designs should be explored in the future. One of the potentially exciting payoffs of using these configurations to observe ET IMRI sources is the ability to test whether the central object of an IMRI is described by the Kerr metric of general relativity. During the inspiral, the CO traces out the geometry of the spacetime of the central object. Hence, the GWs emitted during the inspiral encode a map of the spacetime. [53, 54] showed that any axisymmetric, vacuum spacetime in relativity can be decomposed into mass, M_ℓ, and current, S_ℓ, multipole moment. Ryan [55] went on to show that these multipole moments are redundantly encoded in gravitational wave observables, namely, the periapsis precession frequency, the orbital plane precession frequency and the gravitational wave energy spectrum, for nearly equatorial, nearly circular orbits. Additionally, Hansed [54] showed that all the multipoles of a Kerr black hole are determined by its mass, M, and spin S_1, trough the relation [54]

$$M_\ell + \mathrm{i}S_\ell = M\,(\mathrm{i}a)^\ell\,, \tag{17}$$

where $a = S_1/M$ is the reduced spin of the black hole. Extracting three moments of the spacetime from GW emission, and finding them inconsistent with (17), would suffice to demonstrate that the central object is not a Kerr black hole. Tests of this nature have been conducted for EMRI observations with LISA. Using a kludge model that included a non–Kerr value for the quadrupole moment of the central black hole, Barack and Cutler [56] showed that LISA could measure the quadrupole moment, $Q = -S^2/M$, of the central black hole to an accuracy $\Delta Q/M^3 \sim 10^{-3}$, while simultaneously measuring the mass and spin to an accuracy $\sim 10^{-4}$. In the context of Advanced LIGO, it has been shown that it is possible to measure an 0(1) fractional deviation in the mass quadrupole moment for typical systems [57]. The results we have obtained in this series of papers suggest that ET may improve this estimate by an order of magnitude. Reasons for such expectation include the fact that the SNR of a source at fixed distance will increase by a factor of ten or more, as compared with Advanced LIGO. Furthermore, ET's enhanced sensitivity will

[2] The xylophone configuration consists of two detectors within the same vacuum system, one optimised for low–frequency sensitivity and the second for high–frequency sensitivity.

Model		Statistics of distribution of $\log_{10}(\Delta X)$ for error, ΔX, in parameter $X =$									
		$\ln(m)$	$\ln(M)$	q	t_0	ϕ_0	θ_S	ϕ_S	θ_K	ϕ_K	$\ln(D)$
q=0.9	Mean	-2.91	-3.29	-3.07	-1.65	-0.74	-1.39	-1.26	-0.95	-0.83	-0.89
	St. Dev.	0.196	0.163	0.416	0.157	0.122	0.171	0.269	0.542	0.552	0.410
	L.Qt.	-3.00	-3.34	-3.04	-1.80	-0.79	-1.52	-1.46	-1.32	-1.24	-1.22
	Med.	-2.91	-3.29	-2.95	-1.70	-0.74	-1.38	-1.31	-1.11	-0.97	-1.04
	U. Qt.	-2.77	-3.22	-2.91	-1.60	-0.66	-1.25	-1.10	-0.69	-0.55	-0.61
q=0.3	Mean	-2.85	-3.44	-2.69	-1.96	-0.90	-1.36	-1.22	-0.88	-0.76	-0.81
	St. Dev.	0.362	0.364	0.346	0.386	0.208	0.221	0.304	0.536	0.511	0.458
	L.Qt.	-2.97	-3.70	-2.77	-2.13	-1.00	-1.50	-1.44	-1.29	-1.21	-1.18
	Med.	-2.80	-3.46	-2.67	-1.94	-0.89	-1.36	-1.26	-1.08	-0.93	-0.94
	U. Qt.	-2.76	-3.20	-2.62	-1.85	-0.77	-1.25	-1.08	-0.57	-0.45	-0.49
q=0	Mean	-2.36	-2.81	N/A	-1.97	-0.96	-1.36	-1.21	-0.90	-0.80	-0.83
	St. Dev.	0.388	0.208	N/A	0.444	0.204	0.219	0.316	0.596	0.641	0.473
	L.Qt.	-2.53	-2.92	N/A	-2.15	-1.06	-1.51	-1.44	-1.30	-1.24	-1.22
	Med.	-2.34	-2.82	N/A	-1.93	-0.98	-1.36	-1.26	-1.10	-0.91	-0.95
	U. Qt.	-2.16	-2.70	N/A	-1.89	-0.86	-1.24	-1.07	-0.60	-0.42	-0.48
EOB	Mean	-2.53	-2.87	N/A	-1.99	-1.02	-1.38	-1.25	-0.96	-0.85	-0.85
	St. Dev.	0.187	0.158	N/A	0.203	0.165	0.183	0.274	0.510	0.541	0.385
	L.Qt.	-2.66	-2.97	N/A	-2.10	-1.12	-1.52	-1.45	-1.33	-1.25	-1.18
	Med.	-2.52	-2.86	N/A	-2.00	-1.02	-1.38	-1.28	-1.12	-0.99	-0.92
	U. Qt.	-2.41	-2.77	N/A	-1.86	-0.92	-1.24	-1.09	-0.64	-0.53	-0.58

TABLE IV: As Table II, but now for binary systems with a central IMBH of mass $M = 500M_\odot$.

significantly improve Advanced LIGO's ability to measure multipole moments, as these can be determined with the number of gravitational–wave cycles observed. For instance, for a $1M_\odot + 100M_\odot$ system at leading–order Newtonian approximation, Advanced LIGO will be able to measure ~ 500 cycles until plunge. In sharp contrast, ET will be able to measure up to ~ 25000 at a frequency of 1Hz [58]. Future work on this issue should be conducted to quantify the actual ability of ET to carry out tests of the nature of IMBHs.

There is much science that could be done with ET detections of IMRIs. For instance, a detection of a light black hole at high redshift would be important for constraining light–seed versus heavy–seed models for the formation of structure in the Universe. Based on the results obtained in these papers, ET could detect a significant number of IMRIs involving seed black holes, which will provide constrains on the mass and spin distributions of black hole seeds along with their early accretion history. A more exciting prospect for GW astronomy will be the detection of IMBHs in the centres of globular clusters. ET will test whether IMBHs form at all in these stellar environments. If they do exist, and are not ejected from the host cluster by hardening and eventual recoil, then, according to numerical simulations [49, 50], we may expect numerous lower–mass CO IMRIs into IMBHs, driven by the combination of various mechanisms, i.e., binary exchange processes, gravitational radiation, secular evolution of hierarchical triple systems, and three and four body interactions [10]. Among these various GW sources, stellar mass BH IMRIs into IMBH will be some of the most promising sources of GWs detectable by ET [49]. Additionally, we may expect the IMRI event rate for ET to be as high as a few hundred per year [10, 15].

Our results are a first attempt to explore the precision of IMRI parameter estimation that is achievable with the Einstein Telescope. Our results have been derived using a particular waveform model, which reflects the best of what is currently available, and combines results from both comparable mass binaries and extreme-mass-ratio inspirals. These waveforms are unlikely to be accurate enough to be used in a search to recover source parameters, but they should capture most of the main features of true IMRI waveforms and therefore provide a decent estimate of the level of precision that could be achieved by GW measurements. The waveform models could be improved in various ways, by including conservatives corrections, by generalizing the waveform models to consider both eccentric and inclined orbits to the equatorial plane, and by including the leading order effects of the spin of the smaller object. The EOB model can also now be extended to spinning systems, for circular-equatorial inspirals at least [29]. These will be important improvements to consider in the future in order to confirm our present results, and extend the calculations to eccentric and inclined binary systems.

Model		Statistics of distribution of $\log_{10}(\Delta X)$ for error, ΔX, in parameter $X =$									
		$\ln(m)$	$\ln(M)$	q	t_0	ϕ_0	θ_S	ϕ_S	θ_K	ϕ_K	$\ln(D)$
q=0.9	Mean	-3.57	-4.06	-3.86	-1.85	-0.59	-1.39	-1.27	-0.88	-0.77	-0.90
	St. Dev.	0.268	0.153	0.282	0.147	0.320	0.166	0.243	0.593	0.614	0.455
	L.Qt.	-3.67	-4.13	-3.83	-1.91	-0.83	-1.52	-1.46	-1.31	-1.23	-1.27
	Med.	-3.54	-4.05	-3.77	-1.83	-0.73	-1.38	-1.29	-1.08	-0.94	-1.03
	U. Qt.	-3.42	-3.98	-3.74	-1.76	-0.40	-1.26	-1.12	-0.52	-0.41	-0.61
q=0.3	Mean	-3.56	-4.24	-3.74	-1.94	-0.92	-1.39	-1.24	-0.94	-0.83	-0.95
	St. Dev.	0.162	0.208	0.298	0.204	0.491	0.164	0.266	0.543	0.570	0.410
	L.Qt.	-3.73	-4.25	-3.86	-1.99	-1.22	-1.52	-1.44	-1.32	-1.24	-1.27
	Med.	-3.50	-4.20	-3.76	-1.93	-1.10	-1.38	-1.27	-1.13	-0.99	-1.08
	U. Qt.	-3.43	-4.13	-3.61	-1.78	-0.60	-1.26	-1.10	-0.64	-0.52	-0.72
q=0	Mean	-3.60	-3.97	N/A	-1.98	-0.96	-1.39	-1.27	-0.97	-0.85	-0.95
	St. Dev.	0.189	0.194	N/A	0.241	0.401	0.167	0.257	0.533	0.542	0.396
	L.Qt.	-3.60	-3.97	N/A	-2.20	-1.22	-1.51	-1.46	-1.34	-1.24	-1.26
	Med.	-3.58	-3.93	N/A	-1.96	-1.13	-1.39	-1.29	-1.14	-0.99	-1.06
	U. Qt.	-3.53	-3.91	N/A	-1.90	-0.75	-1.26	-1.13	-0.70	-0.52	-0.72
EOB	Mean	-3.54	-3.90	N/A	-1.97	-1.15	-1.36	-1.24	-0.97	-0.83	-0.86
	St. Dev.	0.187	0.191	N/A	0.252	0.205	0.223	0.292	0.581	0.622	0.469
	L.Qt.	-3.64	-3.99	N/A	-2.10	-1.25	-1.52	-1.45	-1.35	-1.27	-1.22
	Med.	-3.56	-3.92	N/A	-1.98	-1.18	-1.38	-1.29	-1.16	-0.99	-0.97
	U. Qt.	-3.51	-3.87	N/A	-1.91	-1.10	-1.24	-1.08	-0.73	-0.55	-0.61

TABLE V: As Table III, but now for binary systems with a central IMBH of mass $M = 500M_{\odot}$.

Acknowledgments

E.H. is supported by CONACyT. J.G.'s work is supported by the Royal Society.

[1] A. Ori and K. S. Thorne, Phys. Rev. D **62**, 124022 (2000), arXiv:gr-qc/0003032.
[2] B. P. Abbott, R. Abbott, R. Adhikari, P. Ajith, B. Allen, G. Allen, R. S. Amin, S. B. Anderson, W. G. Anderson, M. A. Arain, et al., Reports on Progress in Physics **72**, 076901 (2009), 0711.3041.
[3] H. Grote and the LIGO Scientific Collaboration, Classical and Quantum Gravity **25**, 114043 (2008).
[4] F. Acernese, M. Alshourbagy, P. Amico, F. Antonucci, S. Aoudia, K. G. Arun, P. Astone, S. Avino, L. Baggio, G. Ballardin, et al., Classical and Quantum Gravity **25**, 184001 (2008).
[5] B. P. Abbott, R. Abbott, R. Adhikari, P. Ajith, B. Allen, G. Allen, R. S. Amin, S. B. Anderson, W. G. Anderson, M. A. Arain, et al. (LIGO Scientific Collaboration), Phys. Rev. D **80**, 102001 (2009).
[6] B. P. Abbott, R. Abbott, R. Adhikari, P. Ajith, B. Allen, G. Allen, R. S. Amin, S. B. Anderson, W. G. Anderson, M. A. Arain, et al. (The LIGO Scientific Collaboration), Phys. Rev. D **80**, 102002 (2009).
[7] The LIGO Scientific Collaboration and the Virgo Collaboration, ArXiv e-prints (2010), 1002.1036.
[8] B. Abbott, R. Abbott, R. Adhikari, J. Agresti, P. Ajith, B. Allen, R. Amin, S. B. Anderson, W. G. Anderson, M. Arain, et al., Classical and Quantum Gravity **24**, 5343 (2007), 0704.0943.
[9] M. C. Miller and E. J. M. Colbert, International Journal of Modern Physics D **13**, 1 (2004).
[10] J. R. Gair, I. Mandel, M. C. Miller, and M. Volonteri, ArXiv e-prints (2009), 0907.5450.
[11] J. R. Gair, ArXiv e-prints (2008), 0811.0188.
[12] T. Damour and A. Nagar, ArXiv e-prints (2009), 0906.1769.
[13] S. Babak, H. Fang, J. R. Gair, K. Glampedakis, and S. A. Hughes, *Phys. Rev.* D **75**, 024005 (2007), arXiv:gr-qc/0607007.
[14] E. A. Huerta and J. R. Gair, *Phys. Rev.* D **79**, 084021 (2009), 0812.4208.
[15] E. A. Huerta and J. R. Gair, ArXiv e-prints (2010), 1009.1985.
[16] A. Buonanno, Y. Pan, J. G. Baker, J. Centrella, B. J. Kelly, S. T. McWilliams, and J. R. van Meter, Phys. Rev. D **76**, 104049 (2007), 0706.3732.
[17] A. Buonanno and T. Damour, Phys. Rev. D **62**, 064015 (2000), arXiv:gr-qc/0001013.
[18] C. Kant Mishra, K. G. Arun, B. R. Iyer, and B. S. Sathyaprakash, ArXiv e-prints (2010), 1005.0304.
[19] A. Freise, S. Chelkowski, S. Hild, W. Del Pozzo, A. Perreca, and A. Vecchio, Classical and Quantum Gravity **26**, 085012

Model		Statistics of distribution of $\log_{10}(\Delta X)$ for error, ΔX, in parameter $X =$									
		$\ln(m)$	$\ln(M)$	q	t_0	ϕ_0	θ_S	ϕ_S	θ_K	ϕ_K	$\ln(D)$
C1	Mean	-2.93	-3.49	-2.94	-1.69	-0.59	0.17	0.26	0.54	0.61	0.62
	St. Dev.	0.248	0.354	0.204	0.353	0.212	.719	.736	0.691	0.729	0.634
	L.Qt.	-2.99	-3.68	-3.09	-1.85	-0.65	-0.61	-0.59	0.10	0.15	0.17
	Med.	-2.91	-3.49	-2.94	-1.70	-0.59	0.12	0.30	0.50	0.58	0.56
	U. Qt.	-2.83	-3.30	-2.81	-1.55	-0.54	1.00	1.07	1.03	1.09	1.08
C2	Mean	-2.98	-3.54	-3.04	-1.77	-0.63	-1.16	-1.04	-0.77	-0.68	-0.66
	St. Dev.	0.251	0.336	0.193	0.347	0.205	0.383	0.410	0.590	0.664	0.477
	L. Qt.	-3.02	-3.75	-3.13	-1.91	-0.68	-1.43	-1.36	-1.18	-1.14	-1.02
	Med.	-2.94	-3.54	-3.01	-1.74	-0.61	-1.23	-1.09	-0.92	-0.86	-0.75
	U. Qt.	-2.87	-3.35	-2.90	-1.58	-0.56	-0.97	-0.77	-0.49	-0.32	-0.39
C3	Mean	-3.00	-3.55	-3.06	-1.78	-0.64	-1.33	-1.20	-0.98	-0.83	-0.85
	St. Dev.	0.248	0.316	0.186	0.331	0.203	0.268	0.321	0.580	0.653	0.474
	L. Qt.	-3.04	-3.73	-3.16	-1.95	-0.68	-1.51	-1.45	-1.34	-1.29	-1.20
	Med.	-2.95	-3.54	-3.04	-1.75	-0.61	-1.31	-1.22	-1.15	-1.05	-0.99
	U. Qt.	-2.89	-3.36	-2.90	-1.58	-0.56	-1.19	-1.04	-0.80	-0.57	-0.60
C4	Mean	-3.01	-3.56	-3.09	-1.80	-0.66	-1.33	-1.20	-0.98	-0.84	-0.86
	St. Dev.	0.273	0.322	0.186	0.333	0.233	0.283	0.311	0.570	0.633	0.452
	L. Qt.	-3.06	-3.74	-3.20	-1.95	-0.69	-1.48	-1.45	-1.37	-1.29	-1.23
	Med.	-2.95	-3.54	-3.06	-1.75	-0.61	-1.35	-1.25	-1.16	-1.05	-0.99
	U. Qt.	-2.89	-3.37	-2.92	-1.62	-0.57	-1.24	-1.05	-0.81	-0.58	-0.62
C5	Mean	-3.03	-3.57	-3.11	-1.82	-0.67	-1.38	-1.25	-0.99	-0.86	-0.87
	St. Dev.	0.279	0.320	0.203	0.331	0.232	0.207	0.270	0.591	0.656	0.479
	L.Qt.	-3.05	-3.75	-3.20	-1.95	-0.70	-1.53	-1.45	-1.38	-1.31	-1.24
	Med.	-2.95	-3.55	-3.07	-1.78	-0.62	-1.38	-1.28	-1.20	-1.05	-1.00
	U. Qt.	-2.89	-3.37	-2.93	-1.63	-0.57	-1.25	-1.11	-0.78	-0.58	-0.63

TABLE VI: As Table II, but for binary systems with a central IMBH of spin parameter $q = 0.3$ and assuming four alternative configurations for the detector network, C1-C4, as described in Section II. Configuration C5 is the network of three ETs which has been used for all results elsewhere in this paper.

(2009), 0804.1036.
[20] I. Mandel, ArXiv e-prints (2007), 0707.0711.
[21] J. R. Gair and K. Glampedakis, *Phys. Rev.* D **73**, 064037 (2006), arXiv:gr-qc/0510129.
[22] T. Damour, Phys. Rev. D **64**, 124013 (2001), arXiv:gr-qc/0103018.
[23] T. Damour, P. Jaranowski, and G. Schäfer, Phys. Rev. D **78**, 024009 (2008), 0803.0915.
[24] Y. Pan, A. Buonanno, L. T. Buchman, T. Chu, L. E. Kidder, H. P. Pfeiffer, and M. A. Scheel, Phys. Rev. D **81**, 084041 (2010), 0912.3466.
[25] T. Damour and A. Nagar, Phys. Rev. D **79**, 081503 (2009), 0902.0136.
[26] A. Buonanno, Y. Pan, H. P. Pfeiffer, M. A. Scheel, L. T. Buchman, and L. E. Kidder, Phys. Rev. D **79**, 124028 (2009), 0902.0790.
[27] E. Barausse, E. Racine, and A. Buonanno, Phys. Rev. D **80**, 104025 (2009), 0907.4745.
[28] T. Damour and A. Nagar, Phys. Rev. D **76**, 044003 (2007), 0704.3550.
[29] N. Yunes, A. Buonanno, S. A. Hughes, Y. Pan, E. Barausse, M. C. Miller, and W. Throwe, ArXiv e-prints (2010), 1009.6013.
[30] E. Berti, V. Cardoso, and C. M. Will, Phys. Rev. D **73**, 064030 (2006), arXiv:gr-qc/0512160.
[31] A. Buonanno, G. B. Cook, and F. Pretorius, Phys. Rev. D **75**, 124018 (2007), arXiv:gr-qc/0610122.
[32] L. Rezzolla, P. Diener, E. N. Dorband, D. Pollney, C. Reisswig, E. Schnetter, and J. Seiler, *Astrophys. J.* Lett **674**, L29 (2008), 0710.3345.
[33] P. A. Sundararajan, Phys. Rev. D **77**, 124050 (2008), 0803.4482.
[34] C. O. Lousto and Y. Zlochower, ArXiv e-prints (2010), 1009.0292.
[35] M. Maggiore, *Gravitational Waves* (OXFORD, 2008).
[36] L. Barack and C. Cutler, *Phys. Rev.* D **69**, 082005 (2004), arXiv:gr-qc/0310125.
[37] M. Vallisneri, Phys. Rev. D **77**, 042001 (2008), arXiv:gr-qc/0703086.
[38] L. Wen and Y. Chen, Phys. Rev. D **81**, 082001 (2010), 1003.2504.
[39] S. Fairhurst, ArXiv e-prints (2010), 1010.6192.

[40] P. Ajith and S. Bose, Phys. Rev. D **79**, 084032 (2009), 0901.4936.
[41] M. Luna and A. M. Sintes, Classical and Quantum Gravity **23**, 3763 (2006), arXiv:gr-qc/0601072.
[42] J. R. Gair, I. Mandel, A. Sesana, and A. Vecchio, Classical and Quantum Gravity **26**, 204009 (2009), 0907.3292.
[43] P. Ajith, S. Babak, Y. Chen, M. Hewitson, B. Krishnan, A. M. Sintes, J. T. Whelan, B. Brügmann, P. Diener, N. Dorband, et al., Phys. Rev. D **77**, 104017 (2008), 0710.2335.
[44] S. Sigurdsson and L. Hernquist, Nature (London) **364**, 423 (1993).
[45] G. Schaller, D. Schaerer, G. Meynet, and A. Maeder, *A&AS* **96**, 269 (1992).
[46] M. Freitag, M. A. Gürkan, and F. A. Rasio, *MNRAS* **368**, 141 (2006), arXiv:astro-ph/0503130.
[47] S. D. Murray and D. N. C. Lin, Astrophys. J. **467**, 728 (1996).
[48] N. E. White and J. van Paradijs, *Astrophys. J.* Lett **473**, L25+ (1996).
[49] R. M. O'Leary, F. A. Rasio, J. M. Fregeau, N. Ivanova, and R. O'Shaughnessy, Astrophys. J. **637**, 937 (2006), arXiv:astro-ph/0508224.
[50] Y. Taniguchi, Y. Shioya, T. G. Tsuru, and S. Ikeuchi, *PASJ* **52**, 533 (2000), arXiv:astro-ph/0002389.
[51] M. C. Miller and D. P. Hamilton, Astrophys. J. **576**, 894 (2002), arXiv:astro-ph/0202298.
[52] M. C. Miller and D. P. Hamilton, *MNRAS* **330**, 232 (2002), arXiv:astro-ph/0106188.
[53] R. Geroch, Journal of Mathematical Physics **11**, 2580 (1970).
[54] R. Geroch, Journal of Mathematical Physics **15**, 46 (1974).
[55] F. D. Ryan, *Phys. Rev.* D **52**, 5707 (1995).
[56] L. Barack and C. Cutler, Phys. Rev. D **75**, 042003 (2007), arXiv:gr-qc/0612029.
[57] D. A. Brown, J. Brink, H. Fang, J. R. Gair, C. Li, G. Lovelace, I. Mandel, and K. S. Thorne, Physical Review Letters **99**, 201102 (2007), arXiv:gr-qc/0612060.
[58] L. S. Finn and K. S. Thorne, Phys. Rev. D **62**, 124021 (2000), arXiv:gr-qc/0007074.

Appendix A: Dependence of parameter estimation errors on network configuration

This Appendix contains Tables VII–IX. These Tables show how parameter determination depends on the network configuration. We explore how parameter estimation accuracies are modified for five network configurations, C1–C5. These configurations are, C1: one ET at the geographic location of Virgo; C2: as configuration C1 plus a right–angle detector at the location of LIGO Livingston; C3: as configuration C1 plus another ET at the location of LIGO Livingston; and C4: as configuration C2 plus another right–angle detector in Perth. We will denote the reference 3-ET network as configuration C5.

Model		Statistics of distribution of $\log_{10}(\Delta X)$ for error, ΔX, in parameter $X =$									
		$\ln(m)$	$\ln(M)$	q	t_0	ϕ_0	θ_S	ϕ_S	θ_K	ϕ_K	$\ln(D)$
C1	Mean	-4.01	-4.11	-3.73	-1.58	-0.52	0.40	0.49	0.78	0.87	0.86
	St. Dev.	0.260	0.337	0.206	0.354	0.221	.764	0.748	0.481	0.522	0.373
	L. Qt.	-4.20	-4.35	-3.76	-1.76	-0.70	-0.11	-0.08	0.50	0.61	0.71
	Med.	-4.04	-4.15	-3.68	-1.60	-0.53	0.51	0.62	0.84	0.91	0.94
	U. Qt.	-3.84	-3.93	-3.64	-1.45	-0.35	1.02	1.20	1.14	1.23	1.11
C2	Mean	-4.06	-4.18	-3.83	-1.75	-0.69	-1.19	-1.07	-0.72	-0.63	-0.68
	St. Dev.	0.254	0.341	0.199	0.363	0.165	0.340	0.391	0.520	0.560	0.450
	L. Qt.	-4.24	-4.39	-3.84	-1.87	-0.81	-1.42	-1.39	-1.14	-1.14	-1.08
	Med.	-4.10	-4.21	-3.72	-1.78	-0.72	-1.22	-1.12	-0.86	-0.74	-0.78
	U. Qt.	-3.91	-3.99	-3.66	-1.65	-0.59	-1.03	-0.81	-0.50	-0.30	-0.42
C3	Mean	-4.08	-4.20	-3.85	-1.78	-0.72	-1.36	-1.24	-0.97	-0.84	-0.92
	St. Dev.	0.246	0.331	0.194	0.353	0.159	0.202	0.293	0.510	0.512	0.413
	L. Qt.	-4.24	-4.42	-3.89	-1.89	-0.83	-1.53	-1.46	-1.36	-1.27	-1.28
	Med.	-4.11	-4.25	-3.73	-1.81	-0.75	-1.34	-1.26	-1.18	-0.89	-1.10
	U. Qt.	-3.92	-4.01	-3.69	-1.67	-0.61	-1.22	-1.10	-0.75	-0.57	-0.74
C4	Mean	-4.09	-4.23	-3.85	-1.78	-0.72	-1.39	-1.27	-0.98	-0.85	-0.94
	St. Dev.	0.224	0.304	0.203	0.379	0.157	.180	0.275	0.501	0.509	0.411
	L. Qt.	-4.24	-4.44	-3.89	-1.88	-0.83	-1.49	-1.48	-1.35	-1.31	-1.28
	Med.	-4.12	-4.24	-3.74	-1.77	-0.75	-1.37	-1.28	-1.14	-1.00	-1.09
	U. Qt.	-3.92	-4.02	-3.66	-1.67	-0.61	-1.27	-1.14	-0.75	-0.57	-0.71
C5	Mean	-4.09	-4.23	-3.87	-1.78	-0.73	-1.40	-1.29	-0.99	-0.86	-0.95
	St. Dev.	0.233	0.308	0.198	0.375	0.167	0.179	0.265	0.500	0.543	0.459
	L.Qt.	-4.26	-4.43	-3.91	-1.89	-0.83	-1.53	-1.47	-1.38	-1.30	-1.30
	Med.	-4.11	-4.24	-3.84	-1.77	-0.75	-1.38	-1.31	-1.21	-1.06	-1.14
	U. Qt.	-3.94	-4.04	-3.69	-1.68	-0.63	-1.27	-1.13	-0.75	-0.57	-0.73

TABLE VII: Summary of Monte Carlo results for parameter estimation errors. We show the mean, standard deviation, median and quartiles of the distribution of the logarithm to base ten of the error in each parameter. Results are given for a $m = 1.4M_\odot$ CO inspiralling into a $M = 100M_\odot$ IMBH with spin parameter $q = 0.3$, and assuming four alternative configurations for the detector network, C1–C4, as described above. Configuration C5 is the network of three ETs which has been used for all results elsewhere in this paper.

Model		Statistics of distribution of $\log_{10}(\Delta X)$ for error, ΔX, in parameter $X =$									
		$\ln(m)$	$\ln(M)$	q	t_0	ϕ_0	θ_S	ϕ_S	θ_K	ϕ_K	$\ln(D)$
C1	Mean	-2.67	-3.30	-2.63	-1.68	-0.63	-0.03	0.10	0.37	0.46	0.43
	St. Dev.	0.388	0.399	0.252	0.380	0.242	0.630	0.653	0.545	0.554	0.487
	L. Qt.	-2.75	-3.58	-2.71	-1.99	-0.79	-0.69	-0.63	0.03	0.13	0.11
	Med.	-2.60	-3.30	-2.63	-1.79	-0.61	-0.03	0.11	0.34	0.43	0.36
	U. Qt.	-2.50	-3.06	-2.58	-1.57	-0.47	0.67	0.82	0.73	0.78	0.72
C2	Mean	-2.77	-3.39	-2.66	-1.88	-0.82	-1.12	-0.99	-0.62	-0.54	-0.57
	St. Dev.	0.380	0.383	0.272	0.374	0.241	0.432	0.471	0.530	0.540	0.470
	L. Qt.	-2.90	-3.68	-2.74	-2.06	-0.95	-1.42	-1.34	-1.03	-0.97	-0.94
	Med.	-2.64	-3.43	-2.66	-1.89	-0.83	-1.19	-1.05	-0.77	-0.67	-0.65
	U. Qt.	-2.54	-3.14	-2.60	-1.69	-0.68	-0.97	-0.75	-0.30	-0.15	-0.18
C3	Mean	-2.83	-3.42	-2.68	-1.91	-0.87	-1.32	-1.18	-0.85	-0.74	-0.79
	St. Dev.	0.375	0.372	0.314	0.372	0.224	0.270	0.353	0.512	0.510	0.453
	L. Qt.	-2.98	-3.67	-2.75	-2.09	-0.98	-1.51	-1.43	-1.27	-1.18	-1.14
	Med.	-2.67	-3.45	-2.67	-1.90	-0.89	-1.32	-1.24	-1.05	-0.89	-0.91
	U. Qt.	-2.57	-3.17	-2.61	-1.72	-0.76	-1.20	-1.03	-0.56	-0.42	-0.50
C4	Mean	-2.82	-3.43	-2.68	-1.92	-0.89	-1.34	-1.20	-0.86	-0.75	-0.79
	St. Dev.	0.370	0.370	0.310	0.370	0.221	0.261	0.337	0.510	0.500	0.451
	L. Qt.	-2.94	-3.71	-2.77	-2.12	-0.98	-1.46	-1.41	-1.28	-1.20	-1.17
	Med.	-2.68	-3.47	-2.67	-1.91	-0.88	-1.35	-1.24	-1.06	-0.91	-0.92
	U. Qt.	-2.58	-3.17	-2.61	-1.73	-0.79	-1.26	-1.08	-0.57	-0.41	-0.52
C5	Mean	-2.85	-3.44	-2.69	-1.96	-0.90	-1.36	-1.22	-0.88	-0.76	-0.81
	St. Dev.	0.362	0.364	0.346	0.386	0.208	0.221	0.304	0.536	0.511	0.458
	L.Qt.	-2.97	-3.70	-2.77	-2.13	-1.00	-1.50	-1.44	-1.29	-1.21	-1.18
	Med.	-2.80	-3.46	-2.67	-1.94	-0.89	-1.36	-1.26	-1.08	-0.93	-0.94
	U. Qt.	-2.76	-3.20	-2.62	-1.85	-0.77	-1.25	-1.08	-0.57	-0.45	-0.49

TABLE VIII: As Table VII, but for binary systems with a CO of mass $m = 10M_\odot$, and a central IMBH of mass $M = 500M_\odot$.

Model		Statistics of distribution of $\log_{10}(\Delta X)$ for error, ΔX, in parameter $X =$									
		$\ln(m)$	$\ln(M)$	q	t_0	ϕ_0	θ_S	ϕ_S	θ_K	ϕ_K	$\ln(D)$
C1	Mean	-3.45	-4.13	-3.67	-1.56	-0.33	-0.09	0.01	0.29	0.33	0.30
	St. Dev.	0.184	0.140	0.241	0.286	0.494	0.755	0.753	0.397	0.463	0.404
	L. Qt.	-3.46	-4.16	-3.81	-1.65	-0.65	-0.61	-0.50	0.04	0.06	0.05
	Med.	-3.39	-4.11	-3.69	-1.57	-0.17	0.02	0.09	0.29	0.35	0.31
	U. Qt.	-3.53	-4.09	-3.57	-1.42	0.05	0.46	0.61	0.55	0.64	0.59
C2	Mean	-3.52	-4.19	-3.71	-1.74	-0.80	-1.16	-1.03	-0.67	-0.59	-0.68
	St. Dev.	0.183	0.204	0.251	0.280	0.498	0.389	0.429	0.391	0.460	0.427
	L. Qt.	-3.63	-4.21	-3.85	-1.79	-1.17	-1.45	-1.39	-1.07	-1.02	-1.02
	Med.	-3.41	-4.15	-3.74	-1.70	-0.97	-1.22	-1.07	-0.77	-0.69	-0.76
	U. Qt.	-3.37	-4.11	-3.59	-1.59	-0.43	-0.99	-0.78	-0.35	-0.21	-0.38
C3	Mean	-3.55	-4.21	-3.73	-1.79	-0.90	-1.35	-1.21	-0.92	-0.80	-0.93
	St. Dev.	0.181	0.201	0.243	0.276	0.477	0.210	0.313	0.381	0.450	0.401
	L. Qt.	-3.70	-4.21	-3.87	-1.83	-1.20	-1.53	-1.48	-1.28	-1.19	-1.25
	Med.	-3.42	-4.15	-3.75	-1.75	-1.09	-1.35	-1.24	-1.09	-0.97	-1.05
	U. Qt.	-3.38	-4.11	-3.60	-1.65	-0.61	-1.22	-1.03	-0.62	-0.49	-0.70
C4	Mean	-3.54	-4.22	-3.73	-1.92	-0.91	-1.38	-1.23	-0.92	-0.81	-0.93
	St. Dev.	0.175	0.200	0.235	0.271	0.472	0.191	0.296	0.376	0.420	0.405
	L. Qt.	-3.68	-4.21	-3.86	-1.97	-1.23	-1.51	-1.46	-1.28	-1.23	-1.26
	Med.	-3.42	-4.15	-3.75	-1.91	-1.09	-1.37	-1.25	-1.07	-0.97	-1.03
	U. Qt.	-3.39	-4.12	-3.61	-1.76	-0.60	-1.27	-1.08	-0.64	-0.50	-0.70
C5	Mean	-3.56	-4.24	-3.74	-1.94	-0.92	-1.39	-1.24	-0.94	-0.83	-0.95
	St. Dev.	0.162	0.208	0.298	0.204	0.491	0.164	0.266	0.543	0.570	0.410
	L.Qt.	-3.73	-4.25	-3.86	-1.99	-1.22	-1.52	-1.44	-1.32	-1.24	-1.27
	Med.	-3.50	-4.20	-3.76	-1.93	-1.10	-1.38	-1.27	-1.13	-0.99	-1.08
	U. Qt.	-3.43	-4.13	-3.61	-1.78	-0.60	-1.26	-1.10	-0.64	-0.52	-0.72

TABLE IX: As Table VII, but for binary systems with a central IMBH of mass $M = 500M_\odot$.